Ordered Mixed-Spacer 2D Bromide Perovskites and the Dual Role of 1,2,4-Triazolium Cation

Xiaotong Li, Hao Dong, George Volonakis, Constantinos Stoumpos, Jacky Even, Claudine Katan, Peijun Guo, Mercouri Kanatzidis

Chemistry of Materials DOI: 10.1021/acs.chemmater.2c01432

Ordered Mixed-spacer 2D Bromide Perovskites and The Dual Role of 1,2,4-triazolium Cation

Xiaotong Li,[†] Hao Dong,[‡] George Volonakis,[§] Constantinos C. Stoumpos,[▽] Jacky Even,[‖] Claudine Katan,[§] Peijun Guo,[‡] and Mercouri G. Kanatzidis[*,†]

[†]Department of Chemistry, Northwestern University, Evanston, Illinois 60208, United States
[‡]Department of Chemical and Environmental Engineering, Yale University, New Haven, Connecticut 06511, United States
[§]Univ Rennes, ENSCR, INSA Rennes, CNRS, ISCR (Institut des Sciences Chimiques de Rennes), UMR 6226, Rennes F-35000, France
[‖]Univ Rennes, INSA Rennes, CNRS, Institut FOTON, UMR 6082, Rennes F-35000, France
[▽]Department of Materials Science and Technology, Voutes Campus, University of Crete, Heraklion GR-70013, Greece

Abstract

Two-dimensional (2D) halide perovskites exhibit extraordinary stability and structural diversity because they can incorporate different organic cations (both cage A-site cation and the spacer). Here we report on the behavior of Tz = 1,2,4-triazolium as an A-site cation as well as a spacer cation in new perovskite compounds. We describe the synthesis and structure-property relationships of a new family of hydrogen-bonding stabilized 2D perovskites, $(IPA)_2(Tz)_{n-1}Pb_nBr_{3n+1}$ (n = 1-3) (IPA = isopropylammonium, Tz = 1,2,4-triazolium), which represents the rare example of 2D perovskites incorporating large A-site cation (Tz) that can form both the n = 2 and 3 phases. However, excess of Tz cations can split the n = 2 layers to act as spacer, and combine with another spacer PA (PA = propylammonium) or BA (BA = butylammonium) to form n = 1 structures $(PA)(Tz)PbBr_4$ and $(BA)(Tz)PbBr_4$. These ordered mixed-spacer perovskites with different interlayer distances are unusual because the different spacers tend to stay in the same interlayer. $(IPA)_2(Tz)_{n-1}Pb_nBr_{3n+1}$ all exhibit broad photoluminescence (PL) emission, but for different reasons. For the n = 1 phase, the large octahedral tilting (small Pb-Br-Pb angle) gives rise to the broad emission, while for the n = 2 and 3 phases, the individual octahedral distortion (large distortion index) plays a more important role. For the mixed-spacer $(PA)(Tz)PbBr_4$ and $(BA)(Tz)PbBr_4$, their bandgaps are in between the parent n = 1 compounds ($(BA)_2PbBr_4$ or $(PA)_2PbBr_4$, and $(Tz)_2PbBr_4$). DFT calculations suggest that the band structures of $(PA)(Tz)PbBr_4$ and $(BA)(Tz)PbBr_4$ combine features from both parent compounds yet differ from a simple

superposition. This work demonstrates the dual role of Tz molecules as the A-site cation in multilayer 2D perovskites and as the spacer in ordered mixed-spacer 2D phases.

Introduction

2D perovskites are outstanding semiconductors thanks to their much-improved stability and wide structural and physical property tunability compared to their 3D counterparts over the past several years.[1-5] Unlike other 2D materials that need to be synthesized using high temperature or high vacuum, 2D perovskites can form through self-assembly of the inorganic ions and the organic cations from solution in an ambient atmosphere. Their structures consist of different layers of corner-sharing metal halide octahedra, with small organic cations templating the cuboctahedral void (the cage A-site cations), separated by the larger organic cations called spacers. Different spacers have been incorporated into 2D perovskites, giving rise to the several structural types such as Ruddlesden-Popper (RP) phase,[6] Dion-Jacobson (DJ) phase[7, 8] and the alternating cations (ACI) in the interlayer phase,[9-11] with the general formula of $(A')_2(A)_{n-1}Pb_nX_{3n+1}$ (A' is a +1 cation, A is the cage A-site cation, X is a halide, n is layer-number), $(A'')(A)_{n-1}Pb_nX_{3n+1}$ (A'' is a +2 cation) and $(B)(A)_nPb_nX_{3n+1}$ (B is guanidinium or thiourea), respectively.[9-11] Thus, unlike their 3D analogs, 2D perovskites leave much room for tailored chemical engineering, significantly increasing the structural diversity, property tunability and flexibility of the perovskite family. Recently, Aubrey *et al.* reported direct assembly of 2D heterostructure single crystals of layered perovskites.[12] They used zwitterion taurines to template the growth of two different metal layers or two layers of different structures (connections) of the same metal in single crystals. Others have tried to combine different spacer cations taking advantage of both the RP and DJ phases in solar cells.[13] Still, the exact structure is challenging to determine in thin films. Yan *et al.* reported the mixed alkyl-aryl cations in chiral 2D perovskites.[14] The crystal structure suggests that the alkyl and aryl cations are alternating between the inorganic layers, and the interlayer distance is between the two parent compounds. The 2D perovskites with mixed spacer cations also exhibit different circular dichroism signal than the purely chiral cation analogs. However, there is no existing example of two spacer cations ordering in different layers in 2D perovskites so far.

Another excellent example of this flexibility in 2D perovskites is the ability to exceed the Goldschmidt tolerance.[15] For the 3D perovskites AMX_3 (M is Pb^{2+}, Sn^{2+} or Ge^{2+}), the choice of the A-site cation is limited by the geometric Goldschmidt tolerance factor, $t = (r_A + r_X)/[\sqrt{2}(r_M + r_X)]$, where r_A, r_M and r_X are the effective radii of A^+, M^{2+} and X^- ions, respectively.[16, 17] So far, Cs^+, methylammonium (MA) and formamidinium (FA) have the most

suitable tolerance factor ($0.8< t < 1$) and are most well studied for the Pb and I system. Recently, Methylhydrazinium (MHy) and aziridinium (AzrH) are incorporated into the cage of 3D perovskites as $(MHy)PbX_3$ (X = Br and Cl)[18, 19] and $(AzrH)PbX_3$ (X = I, Br and Cl)[20], expanding the members of A-site cations in 3D perovskites. In 2D perovskites, the tolerance factor is relaxed and larger A-site cations, such as MHy,[21] dimethylammonium (DMA),[22] ethylammonium (EA),[23-25] guanidinium (GA) [22] and isopropylammonium (IPA)[26] fit into the cages of 2D perovskites. Usually, the metal halide bonds are elongated to fit the large cations, and the spacer layers are compressed to compensate for the strain caused by cage expansion.[22, 23, 27] However, there is a limit for the size of the A-site cation using this strategy. In most cases, only one of the layer-number (either $n = 2$ or $n = 3$) can form because of the unique stacking pattern required to stabilize the structure. For example, we have shown that FA and DMA can only form the $n = 2$ structures of $(BA)_2(FA)Pb_2X_7$ [22, 28, 29] and $(BA)_2(DMA)Pb_2X_7$ [22](X = I and Br), while EA and MHy can only form the $n = 3$ phases of $(BA)_2(EA)_2Pb_3X_{10}$ [23, 24](X = I and Br) and $(BA)_2(MHy)_2Pb_3Br_{10}$[21].

To stabilize high-order members n>1 for 2D perovskites with large A cations, one strategy uses hydrogen bonding to introduce additional weak bonding interactions, either between the organic or the organic-inorganic layer interface. Hydrogen bonding is believed to play an important role in templating many (110)-oriented 2D perovskites.[30-32] Certain spacer cations, especially those incorporating multitopic amino groups with different functionalities, can give rise to unusual structural configurations. For example, besides the ACI phase, GA can also form (110)-oriented 2D perovskites $(GA)_2MI_4$ (M = Pb^{2+} and Sn^{2+}) by itself,[33] or (210)-oriented 2D perovskites $(FA)(GA)PbI_4$ combined with FA[34]. FA and AA (acetamidinium) can also form (110)-oriented 2D perovskite $(FA)_2PbBr_4$ [35]and $(AA)_2PbBr_4$[36]. Another small cation, 1,2,4-triazolium (Tz) can serve as spacer and form (100)-oriented 2D perovskite $(Tz)_2PbX_4$ (X = Br, Cl),[36] but it only forms 1D structure for the iodide. Most $n = 1$ 2D perovskites with small spacer cations have tilted octahedra with small Pb-X-Pb angles, since they can form directional hydrogen bonds between the primary amino group and the bridging (or terminal) halide atoms. Nevertheless, there are exceptions to this general rule, for example, in $(MHy)_2PbX_4$ (X = I, Br) where the Pb-X-Pb angles are close to 180°.[37, 38] The nearly undistorted lattice in $(MHy)_2PbX_4$ may result from the lack of directional bonding due to temperature-induced dynamic distribution of NH_2 and NH_2^+ donor group. Tz and GA together can form a 3D structure of $(GA)_{0.5}(Tz)_{0.5}SnI_3$, where both Tz and GA are inside the perovskite cages ordered in such a way that each layer has only one kind of cation.[39]

These results suggest that Tz can serve as both the spacer and the A-site cations for perovskites. Its ability to form multiple hydrogen bonds suggests that it can form a variety of different structures.

In this work, we present different structures formed by combining Tz with other spacer cations. Tz can play a dual role here: it can serve either as the A-site cage cation or as the spacer. With isopropylammonium (IPA), it can form the homologous series of $(IPA)_2(Tz)_{n-1}Pb_nBr_{3n+1}$ (n = 1-3), where Tz is the A-site cation inside the perovskite cage, and IPA is the spacer separating the inorganic octahedra. The n = 1 phase, $(IPA)_2PbBr_4$, has small Pb-Br-Pb angles, caused by the strain induced by the small IPA spacer. By contrast, both the n = 2 and 3 phases have large Pb-Br-Pb angles, and the Pb-Br bonds are severely elongated to accommodate the large A-site cation Tz. Overall, the structures are held together by strong hydrogen bonds. When Tz cation is combined with other spacer cations such as propylammonium (PA) or butylammonium (BA), they form the mixed-spacer 2D perovskites. Like in the single-spacer n = 1 $(Tz)_2PbBr_4$ structure, in the mixed-cation n = 1 compounds $(PA)(Tz)PbBr_4$ and $(BA)(Tz)PbBr_4$, Tz plays the role of a spacer. In $(PA)(Tz)PbBr_4$ and $(BA)(Tz)PbBr_4$, the layers separated by PA (BA) have larger interlayer distances compared to those next to Tz. Therefore, the two spacer cations are located in different interlayers and there are two distinct interlayer distances within a single n=1 structure, which is structurally different from the mixed-spacer 2D perovskites with one interlayer distance[14]. The $(IPA)_2(Tz)_{n-1}Pb_nBr_{3n+1}$ series all exhibit broad emission at room temperature with a full width at half maximum (FWHM) around 0.8 eV, while the PL for $(PA)(Tz)PbBr_4$ is much narrower (FWHM ≈ 0.1 eV). This is because $(IPA)_2PbBr_4$ exhibits large octahedral tilting (small Pb-Br-Pb angle), and $(IPA)_2(Tz)Pb_2Br_7$ and $(IPA)_2(Tz)_2Pb_3Br_{10}$ have large octahedral distortion (large distortion index), and either of them can lead to broad emission. Neither of these two structural features is present in $(PA)(Tz)PbBr_4$, so it exhibits narrow emission. The bandgap of $(PA)(Tz)PbBr_4$ is in between the two parent compounds $(PA)_2PbBr_4$ and $(Tz)_2PbBr_4$.

Experimental Section

Starting Materials: $PbBr_2$ (98%), 1,2,4-triazole (98%), propylamine (99%), isopropylamine (99.5%), butylamine (99.5%), hydrobromic acid (48 wt % in H_2O, distilled, stabilized, 99.95%), and hypophosphorous acid solution (50 wt % in H_2O) were purchased from Sigma-Aldrich.

$(Tz)_2PbBr_4$[36] and $(BA)_2PbBr_4$[40] were synthesized using the methods reported in the literature.

$(IPA)_2PbBr_4$. An amount of 4 mmol $PbBr_2$ (1468 mg) was dissolved in 3 mL concentrated HBr under heating at 120 °C and stirring for 10 min. In a separate vial, 8 mmol (654.9 μL) isopropylamine (IPA) was added to 0.5 mL H_3PO_2 solution under stirring. The neutralized IPA was then added to the HBr solution under heating and stirring until a clear solution was obtained. Then the hot plate was turned off, and the solution was cooled to room temperature until the white crystals completely precipitated in one day. The crystals were separated by vacuum filtration and dried on the filtration funnel for a further 30 min. Yield: 1304.4 mg, 50.4% based on Pb.

$(IPA)_2(Tz)Pb_2Br_7$. An amount of 8 mmol $PbBr_2$ (2936 mg) and 4 mmol 1,2,4-triazole (Tz) (276 mg) was dissolved in 3 mL concentrated HBr under heating at 120 °C and stirring for 10 min. In a separate vial, 14 mmol (1146.2 μL) isopropylamine (IPA) was added to 0.5 mL H_3PO_2 solution under stirring. The neutralized IPA was then added to the HBr solution under heating and stirring until a clear solution was obtained. Then the hot plate was turned off, and the solution was cooled to room temperature until the light-yellow crystals completely precipitated in one day. The crystals were separated by vacuum filtration and dried on the filtration funnel for a further 30 min. Yield: 2059.7 mg, 44.2% based on Pb.

$(IPA)_2(Tz)_2Pb_3Br_{10}$. An amount of 8 mmol $PbBr_2$ (2936 mg) and 3 mmol 1,2,4-triazole (Tz) (207 mg) was dissolved in 3 mL concentrated HBr under heating at 120 °C and stirring for 10 min. In a separate vial, 4 mmol (327.5 μL) isopropylamine (IPA) was added to 0.5 mL H_3PO_2 solution under stirring. The neutralized IPA was then added to the HBr solution under heating and stirring until a clear solution was obtained. Then the hot plate was turned off, and the solution was cooled to room temperature until the yellow crystals completely precipitated in one day. The crystals were separated by vacuum filtration and dried on the filtration funnel for a further 30 min. Yield: 564.4 mg, 12.6% based on Pb.

$(PA)(Tz)PbBr_4$. An amount of 4 mmol $PbBr_2$ (1468 mg) and 2 mmol 1,2,4-triazole (Tz) (138 mg) was dissolved in 4 mL concentrated HBr under heating at 120 °C and stirring for 10 min. In a separate vial, 2 mmol (164.4 μL) propylamine (PA) was added to 0.5 mL H_3PO_2 solution under stirring. The neutralized PA was then added to the HBr solution under heating and stirring until a clear solution was obtained. Then the hot plate was turned off, and the solution was cooled to room temperature until the white crystals completely precipitated in one day. The crystals were separated

by vacuum filtration and dried on the filtration funnel for a further 30 min. Yield: 1157.3 mg, 44.0% based on Pb.

(BA)(Tz)$PbBr_4$. An amount of 4 mmol $PbBr_2$ (1468 mg) and 2.5 mmol 1,2,4-triazole (Tz) (172.5 mg) was dissolved in 3 mL concentrated HBr under heating at 120 °C and stirring for 10 min. In a separate vial, 1.5 mmol (148.5 μL) butylamine (BA) was added to 0.5 mL H_3PO_2 solution under stirring. The neutralized BA was then added to the HBr solution under heating and stirring until a clear solution was obtained. Then the hot plate was turned off, and the solution was cooled to room temperature until the white crystals completely precipitated in one day. The crystals were separated by vacuum filtration and dried on the filtration funnel for a further 30 min. Yield: 679.4 mg, 25.3% based on Pb.

$(PA)_2PbBr_4$. An amount of 1 mmol $PbBr_2$ (367 mg) was dissolved in 2 mL concentrated HBr under heating at 120 °C and stirring stirred for 10 min. In a separate vial, 2 mmol (164.4 μL) propylamine (PA) was added to 0.5 mL H_3PO_2 solution under stirring. The neutralized PA was then added to the HBr solution under heating and stirring until a clear solution was obtained. Then the hot plate was turned off, and the solution was cooled to room temperature until the white crystals completely precipitated in one day. The crystals were separated by vacuum filtration and dried on the filtration funnel for a further 30 min. Yield: 279.5 mg, 43.2% based on Pb.

Results and Discussion

Synthesis. Synthesis of the n = 1 phases $(IPA)_2PbBr_4$ (IPA = isopropylammonium), $(Tz)_2PbBr_4$ (Tz = 1,2,4-triazolium), $(PA)_2PbBr_4$ (PA = propylammonium) and $(BA)_2PbBr_4$ (BA = butylammonium) utilized stoichiometric ratio (2:1) of the spacer cations and $PbBr_2$. But for the $(IPA)_2(Tz)Pb_2Br_7$ (n = 2) and $(IPA)_2(Tz)_2Pb_3Br_{10}$ (n = 3), off-stoichiometric ratios were used to obtain pure phases. Usually, during the synthesis of 2D perovskites, the solubility of the spacer cation is lower than that of the A-site cation in hydrohalic solutions. But in this case, IPA is more soluble than Tz in HBr. If we use a stoichiometric ratio for the synthesis of the n = 2 phase, the n = 3 phase, which has a larger proportion of Tz would also precipitate out. Therefore, we added an extra amount of IPA (IPA: Tz: $PbBr_2$ = 14: 4: 8) to prevent the co-precipitation of the n = 3 phase. When we reduced the amount of IPA (e.g., IPA: Tz: $PbBr_2$ = 5: 4: 8), a mixture of the n = 3 and $(Tz)_2PbBr_4$ formed because $(Tz)_2PbBr_4$ is less soluble, so we reduced the amount of Tz as well to obtain the pure n = 3 phase. This might seem counterintuitive because the n = 3 phase has a larger ratio of Tz than the n = 2 phase. In general, for the synthesis of 2D perovskites, the phase whose solubility is closest to that of the cation concentrations in solution forms and precipitates out first.[5] Therefore, a balance between the concentration of Tz and IPA is needed. For n = 2, the stoichiometric ratio for IPA: Tz is 2:1, whereas for n = 3 the ratio is 1:1. We then fine-tuned around those ratios until we obtained the pure phases. We find that only the combination of the correct ratio and concentration can lead to the desired pure phases. The color of the crystal changes from white ($(IPA)_2PbBr_4$) to light-yellow for both n = 2 and 3 phases. The powder X-ray diffraction (PXRD) patterns of the n = 1 – 3 phases are shown in Figure S1. Similar to other 2D perovskite series,[6, 41] the number of the low-angle peaks below 2θ = 14° are indicative of the layer-number. The n = 2 phase has two low-angle peaks and the n = 3 phase shows three. The absence of other Bragg peaks below 2θ = 14° and the fact that they match well with the calculated patterns suggest that we have pure phases of the desired n value.

For the synthesis of mixed-spacer n = 1 compounds $(PA)(Tz)PbBr_4$ and $(BA)(Tz)PbBr_4$, a balance between the concentration of PA (BA) and Tz is also necessary to get the pure phases. Starting with a 1: 1 ratio for PA and Tz yields the desired phase because the solubility of PA and Tz in HBr happens to be similar. However, using 1: 1 ratio for BA and Tz, a $(BA)_2PbBr_4$ second phase would also precipitate out because BA is less soluble (since it has a larger non-polar carbon chain component) than PA (Tz). We tried different ratios of BA and Tz but could not obtain a pure

phase for $(BA)(Tz)PbBr_4$, because each time, either $(BA)_2PbBr_4$ or $(Tz)_2PbBr_4$ phase would precipitate out together with the desired phase, and the 2.5: 1.5 ratio for BA: Tz in the experimental section is the one that gives the least amount of the second phase so far. This suggests that a proper balance for BA and Tz is more challenging to obtain, possibly due to the much greater thermodynamic stability of the parent compounds, and further optimization is needed to get a pure phase

Crystal structures. The crystal structures of the $(IPA)_2(Tz)_{n-1}Pb_nBr_{3n+1}$ (n = 1–3) are shown in Figure 1 and their refinement data is shown in Table 1. The n = 1–3 phases adopt the space group of *Cc*, *C*2 and $P2_1$, respectively. They all belong to the Ruddlesden-Popper structure type. The n = 1 phase has the inorganic layers of corner-sharing octahedra separated by the IPA spacer cations, and the octahedra in the adjacent layers are staggered by half an octahedron length. From the side view (Figure 1a), the octahedra are not tilted in the out-of-plane direction, although the top view (Figure 1d) shows that the octahedra are heavily tilted in the in-plane direction. In an un-tilted structure (such as in Figure 1e), the adjacent four Pb atoms form a perfect square. Because of the small size and irregular shape of IPA, the octahedra in the n = 1 phase needs to be tilted to accommodate it. Two opposite Pb-Br-Pb bonds are pushed out, and the other two are pulled in, so a rhombus-shaped void is formed instead (Figure 1d).

For the n = 2 phase, two layers of octahedra form cuboctahedral cages, which are occupied/ templated by the Tz cations, and the IPA cations locate between the inorganic layers as spacers. It is worth pointing out that the configuration of the IPA cation is identified by the electron density of C and N atoms, while the Tz cation is disordered. Because of this, all the bond lengths and bond angles of the Tz cation were fixed, and the rigid Tz ring was left to refine until it converged to the most stable orientations. From Figure 1b, e, we can see that the octahedra are neither tilted in-plane nor out-of-plane. Considering the perovskite cage (Figure 1g), strong hydrogen-bonding can be observed, which is apparently responsible for the stabilization of this unique structure. The distances between the N-H of Tz and the axial Br atoms are 2.29 Å and 3.22 Å (Figure 1g), respectively. The distances between the N-H of IPA and the equatorial Br atoms are 2.83 Å and 2.98 Å, respectively. It is worth pointing out that even though 1,2,4-triazole has three N atoms, only the 4 position can be protonated to meet the requirement of Huckel's rule (4n+2 rule) for aromaticity[42] (molecular structure of Tz shown in Figure 1b). Because of the limit of the symmetry

element, the 1- and 2- position N atoms are symmetry-related by the C2 axis. We keep both protonated and assign half occupancy for the 1- and 2-position H atoms to match with their experimental formula. But, only one of them can be protonated for a given molecule (+1 charge).

For the n = 3 phases, there are three layers of octahedra, whose cages are occupied by Tz, and the inorganic slabs are separated by the IPA cations. From the side view of one direction (Figure 1c), the first layer is tilted out-of-plane. From another direction (Figure 1h), the third layer is tilted. Comparing the distortion among the layer, the inner layer is the least tilted. From the top view (Figure 1f), the first and second layers cannot overlap (unlike the typical structural motif in Figure 1e). This tilting can also be observed in Figure 1h, i. The Pb atoms of the outer layer octahedra are clearly off-centered. The structure is also stabilized by hydrogen bonding. Because of the reduced unit cell symmetry, now the five atoms of Tz are independent, and we can clearly see that only one of the 1 and 2-position N atoms is protonated. The distances between the C-H and Br atoms are shown in Figure 1h and the distances between the N-H and Br atoms are shown in Figure 1i. It is rare in the literature for 2D perovskites to incorporate large A-site cation to form both the n = 2 and n = 3 phases.

The Pb-Br-Pb angles and Pb-Br bond lengths can influence the properties of the 2D perovskites.[22, 43, 44] The octahedra of the n = 1 phase are most tilted, so they have the smallest Pb-Br-Pb angles. For the n = 2 phase, the octahedra are barely tilted, so its Pb-Br-Pb angles are the largest and close to 180°. For the n = 3 phase, the outer layer is more tilted than the inner layer, and its Pb-Br-Pb angles are in between the n = 1 and n = 2 phase (Table S1). As for the Pb-Br bond length, usually, the bonds are elongated to accommodate the large A-site cation. The bond length can be categorized into the axial bond length in the stacking direction and the equatorial one parallel to the layers. The axial bond can be further categorized into the internal one which is next to the A-site cation, and the external one which is close to the spacer. For the n = 2 phase, the internal axial Pb-Br bond length is elongated (3.19 Å), while the external one is shortened (2.78 Å) (Table S2). This is because the spacer layer exhibits a compressive strain to compensate the expansion of the inorganic cage.[22, 23, 27] Similar trends are also observed for the n = 3 phase, where the internal Pb-Br bond lengths are significantly elongated (3.49 and 3.11 Å). In contrast, the external ones are contracted (2.83 and 2.77 Å) (Table S2). The equatorial Pb-Br bond length change is not as obvious as the axial ones.

We can also calculate the distortion level of each octahedron as defined by the distortion index (D) and bond angle variance (σ^2) using the Vesta software[45, 46]. The D and σ^2 are defined by equation (1) and (2), which show the difference between each Pb-Br bond length l_i and the average value l_{av} and the deviation of Pb-Br-Pb angles from 90°. The n = 2 and 3 phases exhibit a much larger (at least twice) distortion index than the n = 1 phase (Table 2), suggesting that the octahedra are distorted to accommodate the large A-site cation.

$$D = \frac{1}{6}\sum_{i}^{6}\frac{|l_i - l_{av}|}{l_{av}} \qquad (1)$$

$$\sigma^2 = \sum_{i=1}^{12}(\theta_i - 90)^2/11 \qquad (2)$$

With the Tz cation and different spacers (PA = propylammonium, BA = butylammonium), new mixed-spacer n = 1 structures ((PA)(Tz)$PbBr_4$ and (BA)(Tz)$PbBr_4$) can form with two layers of Tz between adjacent inorganic layers, and two layers of PA or BA separating another layer (Table 3, Figure 2a, c). The configurations of the Tz and PA (BA) cations are directly determined by the electron density of the C and N atoms. This interesting structure is held together by strong hydrogen bonding. The distances between the N-H of both the triazolium and primary ammonium cations and the Br atoms are around 2.5 Å (Figure 2b, d). The adjacent Tz cations in the same layer adopt a face-to-edge configuration, and the N-H···N distance is around 2.8 Å. This suggests that besides the hydrogen bonding, the N-H··· π interaction between the Tz cations may also contribute to stabilizing the structure.[47]

The structure of (PA)(Tz)$PbBr_4$ can be derived from the hypothetical $(PA)_2(Tz)Pb_2Br_7$ by inserting an extra layer of Tz cations along with a Br^- ion to separate it into two different layers. Two Tz cations, instead of one, are needed to balance the charge in this compound, thus, the Tz cation performs the role of a spacer cation. The interlayer distances, defined by the distance between two planes crossing the terminal Br atoms, are 3.8 Å for the Tz layers and 6.4 Å for the PA layers (Figure 2b). For the BA cations, the interlayer distance is slightly larger (7.5 Å) due to the longer cation length (Figure 2d). Interestingly, the octahedra next to the Tz layers are almost eclipsed, resembling the stacking pattern of the Dion-Jacobson phase. The slabs around the PA (BA) layers are staggered by half an octahedron, which is the same as in the Ruddlesden-Popper phases. Their structures (interlayer distances and stacking patterns) are similar to those of $(Tz)_2PbBr_4$ and $(PA)_2PbBr_4$, respectively, as shown in Figure S2. However, the degree of tilting of the octahedra

is in the middle of the one found in two parent compounds. $(Tz)_2PbBr_4$ has a large Pb-Br-Pb angle of 166.0°, while the average Pb-Br-Pb angle for $(PA)_2PbBr_4$ is much smaller (153.8°). The average Pb-Br-Pb angle for $(PA)(Tz)PbBr_4$ is in between the two parent compounds (161.2°). Both the inorganic layers next to the Tz or the PA spacer have similar Pb-Br-Pb angles. Interestingly, the distortion index of $(PA)(Tz)PbBr_4$ is larger than those of the two parent compounds (Table 2). This is because there is a lattice mismatch between $(Tz)_2PbBr_4$ and $(PA)_2PbBr_4$,[27] and the octahedra are distorted to accommodate this strain. $(BA)(Tz)PbBr_4$ also exhibits similar structural features (Table 2, 4).

These mixed-spacer $n = 1$ structures represent the firstexamples of two different spacers ordering between the inorganic metal halide perovskite layers and creating different interlayer distances. It defines a new type of $n = 1$ superposition with a double motif along the stacking axis. We shall point out that these ordered mixed structures are not the simple superpositions of the motifs of the parent phases. For example, Tz cations in $(PA)(Tz)PbBr_4$ present a tilting pattern that is different from the one in pure $(Tz)_2PbBr_4$. Usually, when two similar cations are mixed in 2D perovskites (crystals and films), they are disordered and cannot be distinguished by single-crystal X-ray diffraction.[48, 49] One exception is $(5FPEA{\cdot}NEA)SnI_4$, (5FPEA = 2,3,4,5,6-pentafluorophenethylammonium, NEA = 2-naphthyleneethylammonium), which is stabilized by the fluoroaryl-aryl interaction between the two organic cations.[48] Even though the cations are not fully resolved by single-crystal XRD, the authors proposed that each of the two spacer layers consists of the same type of organic cation,[48] with one of them interacting with the top layer and the other close to the bottom layer, and there is only one interlayer distance. Recently, Yan *et al.* reported the crystal structures of (S/R-MePEA)(PA)$PbBr_4$ and (S/R-MePEA)(BA)$PbBr_4$ (MePEA=β-methylphenethylammonium), which incorporated ordered alkyl and aryl ammonium cations.[14] When 1:1 ratio of the alkyl and aryl ammonium cations are incorporated into the structure, the spacers are alternating within the same layer, and the inorganic layers only exhibit one interlayer d-spacing, which is in between the two parent compounds. This is because the strong C-H$\cdots\pi$ interactions make the spacer cations more interdigitated, so the interlayer d-spacing is smaller than (S/R-MePEA)$_2PbBr_4$. Other related examples are $(C_6F_5C_2H_4NH_3)_2SnI_4{\cdot}(C_6H_6)$ and $(C_6H_5C_2H_4NH_3)_2SnI_4{\cdot}(C_6F_6)$, which involve 2,3,4,5,6-pentafluorophenethylammonium ($C_6F_5C_2H_4NH_3^+$) or phenethylammonium ($C_6H_5C_2H_4NH_3^+$) as spacers and intercalated

phenyl(C_6H_6) or perfluorophenyl(C_6F_6) molecules.[50] But the intercalated molecules cannot be recognized as spacers in these cases.

This difference can be seen from the PXRD patterns (Figure 3), which show the periodicity of the inorganic layers. It is worth to note that there is a significant preferred orientation for the (400) peak, but all the peak positions match with the calculated ones. For (5FPEA·NEA)SnI_4,[48] its first PXRD peak occurs at 2θ ~ 5°, corresponding to a d-spacing of ~18 Å, which matches with the stacking axis for a primitive cell or ½ of it for the C-centered cell. This suggests that the stacking pattern repeats around every 18 Å. For (S/R-MePEA)(PA)$PbBr_4$ and (S/R-MePEA)(BA)$PbBr_4$, there is also only one set of peaks in the PXRD, indicating one interlayer distance.[14] For (PA)(Tz)$PbBr_4$, there is a small peak at ~2θ = 4°, corresponding to a d-spacing of ~22 Å ((200) plane), which is the sum of the d-spacing of $(PA)_2PbBr_4$ (12.4 Å) and $(Tz)_2PbBr_4$ (9.8 Å). The unit cell consists of two different types of packings, giving rise to a longer stacking axis. The second peak corresponding to the (400) plane is stronger, corresponding to a d-spacing of ~11 Å, and the third peak belongs to the (600) plane.

Optical properties. The absorption spectra of the $(IPA)_2(Tz)_{n-1}Pb_nBr_{3n+1}$ (n = 1 – 3) series are shown in Figure 4a. The bandgap decreases from 2.95 eV for n = 1 phase to 2.90 eV for the n = 2 phase and 2.70 eV for the n = 3 phase. The bandgap reduction mainly comes from the decrease of the quantum confinement effect, but it is not as significant as in the standard 2D perovskites.[4, 5] Specifically, $(IPA)_2(Tz)Pb_2Br_7$ and $(IPA)_2(Tz)_2Pb_3Br_{10}$ still exhibit larger bandgaps than $(BA)_2(MA)Pb_2Br_7$ and $(BA)_2(MA)_2Pb_3Br_{10}$, respectively[51, 52]. Since the average Pb-Br-Pb angles of the first two are larger than the latter (Table S4), the increased bandgaps should not originate from the tilting of the octahedra. The larger bandgap is mainly because the Pb-Br bonds are significantly elongated to accommodate the large Tz cation inside the cage, so there is reduced Pb s- and Br p-orbital overlap, leading to the stabilization of their antibonding valence edges and in turn, the higher bandgaps.[22] Besides, the large distortion of each individual octahedron can also lead to electronic band-narrowing and higher bandgap (Table S4).[53]

The low-frequency Raman spectra of the $(IPA)_2(Tz)_{n-1}Pb_nBr_{3n+1}$ (n = 1 – 3) phases are shown in Figure 4b. They all exhibit a broad, diffuse central peak at 0 cm^{-1}. These spectra resemble those of 3D perovskites at room temperature and suggest that the lattice is dynamically disordered and anharmonic.[54, 55] It has been shown previously that the diffuse character of the Raman spectra are

even more significant for 2D perovskites with larger A-site cations, since the Pb-X bonds are elongated and the lattice becomes softer.[22] Since their structures are distortive, the lattice is even more anharmonic with characteristics of a fluid.

The photoluminescence (PL) of the $(IPA)_2(Tz)_{n-1}Pb_nBr_{3n+1}$ (n = 1-3) compounds and the integrated PL spectra are shown in Figure 4c. They are all relatively broad, and the peak positions are red-shifted compared to the absorption spectra, except for n = 3. For the n = 3 phase, the PL curve exhibits a small peak at ~2.8 eV, which matches with the exciton peak in the absorption spectrum. It also shows a broad shoulder at lower energy. Their full width at half maximum (FWHM) is around 0.8 eV at room temperature. To explore the origin of the broad emission (shoulder) peaks, we measured the temperature-dependent PL for these three compounds from room temperature down to liquid-N_2 temperature (Figure 5). For the n = 1 and 2 phases, the peak shifted to lower energy as the temperature decreased, and their FWHM also decreased (Figure S3). For the n = 3 phase, the position of the small sharp peak almost remains unchanged in the entire temperature range, while the shoulder clearly shifts to lower energy and becomes a distinct peak as temperature decreases. The FWHM of the n = 3 phase first increases with cooling, mainly because the shoulder is shifted to the lower energy, then it starts to decrease as the shoulder becomes a distinct peak. The average PL lifetimes of these samples were extracted from the biexponential decay fitting, and they are all below 0.1 ns at room temperature. As the temperature cools, the PL lifetime becomes significantly longer (by two orders). The n = 3 phase exhibits a shorter lifetime than the n = 1 and 2 phases at all temperature ranges (Figure 5).

The broad emission of the $(IPA)_2(Tz)_{n-1}Pb_nBr_{3n+1}$ (n = 1-3) series can be well correlated with their structural features, such as significant distortion and small Pb-Br-Pb angles. Generally, the broad emissions in halide perovskites are attributed to the large inter-octahedral tilting (small Pb-X-Pb angles)[40] as well as large intra-octahedral distortion (large distortion index). [56] In the present case, the n = 1 phase has the smallest Pb-Br-Pb angles in this series, which is smaller than most of the reported 2D perovskites, presumably because of the small size of IPA, so it exhibits a broad emission. The n = 2 and n = 3 phases have relatively large Pb-Br-Pb angles, but they still exhibit broad emission. A recent report suggests that large intra-octahedral distortion can also give rise to broad emission.[56] However, the distortion of each octahedron is usually convoluted with the inter-octahedral distortion (tilting of the octahedra/ Pb-X-Pb angles). For $(IPA)_2(Tz)Pb_2Br_7$, its Pb-

Br-Pb angle is close to 180° (176.98°), but it has large distortion index, which suggests that the intra-octahedral distortion alone can lead to broad emission. The role of the bond angle variance (σ), however, is less significant since both structures with small σ ($(IPA)_2(Tz)Pb_2Br_7$) or large σ ($(IPA)_2(Tz)_2Pb_3Br_{10}$) can exhibit broad PL.

The absorption spectra of the mixed-spacer n = 1 structures $(PA)(Tz)PbBr_4$ and $(BA)(Tz)PbBr_4$ are shown in Figure 6 and are compared with their parent compounds $(Tz)_2PbBr_4$,$(PA)_2PbBr_4$ and $(BA)_2PbBr_4$. The bandgap of $(PA)(Tz)PbBr_4$ is in between its parent compounds (Figure 6). As discussed above, the Pb-Br-Pb angles in $(PA)(Tz)PbBr_4$ lie between those observed in $(PA)_2PbBr_4$ and $(Tz)_2PbBr_4$.Therefore, its bandgap is still determined by the inorganic layers (Pb-Br-Pb angles). The PL spectrum (FWHM ~ 0.1 eV) (Figure S4) of $(PA)(Tz)PbBr_4$ is significantly narrower than those of the $(IPA)_2(Tz)_{n-1}Pb_nBr_{3n+1}$ (n = 1 – 3) series (FWHM ~0.8 eV), since it neither has large octahedra tilting (small Pb-Br-Pb angle is 161.2°) nor large distortion index (D is 0.01). Its σ is larger than $(IPA)_2PbBr_4$ and $(IPA)_2(Tz)Pb_2Br_7$, which suggests that σ plays a smaller role in the PL broadness.

Electronic structure. The calculated electronic band structures of the n =1, 2 and 3 $(IPA)_2(Tz)_{n-1}Pb_nBr_{3n+1}$ series are shown in Figure S5. Density-functional theory (DFT) calculations using the PBE exchange-correlation (xc) functional reproduce well the measured bandgap trend across the series, and as expected, all compounds clearly show a two-dimensional electronic character, exhibiting flat electronic bands along the stacking direction. More interestingly, we set to analyze the effects of the ordered mixed spacers by investigating the electronic structure of $(PA)_2PbBr_4$, $(Tz)_2PbBr_4$ and the new $(PA)(Tz)PbBr_4$, as shown in Figure 7. The calculated bandgaps by employing the PBE0 hybrid xc-functional are 3.13, 2.90, and 2.98 eV, for $(PA)_2PbBr_4$, and $(Tz)_2PbBr_4$ and $(PA)(Tz)PbBr_4$, respectively. These are in a reasonably good agreement with the experimental data and also find the bandgap of $(PA)(Tz)PbBr_4$ well in between the two parent compounds, as reported above.

Comparing the band dispersion along the stacking direction (Z-Γ) for the two parent compounds $(PA)_2PbBr_4$ and $(Tz)_2PbBr_4$, we can see that there is clearly some type of interlayer interaction for the latter. This feature can be quantified by calculating the charge carrier effective masses, which are summarized in Table 5. In fact, for $(PA)_2PbBr_4$ along the long axis, the calculated carrier masses are more than 100-fold heavier with respect to the in-plane directions, while for $(Tz)_2PbBr_4$

the effective masses along the in-plane and out-of-plane directions vary within one order of magnitude. Such interaction also splits the two degenerate bands at the band edges of $(Tz)_2PbBr_4$ by 80 and 60 meV at the valence band maximum (VBM) and the conduction band minimum (CBM), respectively (Figure S6b). Plotting the pseudo-charge density at the band edges confirms that the lower, more stable bands corresponding to the interlayer bonding interaction (i.e. the sign of the outer orbital of the apical halogens are the same in Figure S7b), while the upper (less stable) bands are of antibonding character across the interlayer. Hence, as shown in Figure S7a, for $(Tz)_2PbBr_4$ there are two observable peaks in the imaginary part of the calculated dielectric function of the material that are separated by 140 meV, which correspond to the symmetry-allowed optical transitions between states of different parity (i.e. from bonding and antibonding states of the VBM to the respective states of the CBM). Consequently, the $(Tz)_2PbBr_4$ adjacent layers are (weakly) interacting, which can be related to the interlayer distance (~3.8 Å) being close to twice the van der Waals radii of Br (3.7 Å) and can be a positive feature for charge transport across its layers.[8]

Moving on to mixed-spacer structure $(PA)(Tz)PbBr_4$, we identify two distinct splits at the band extrema (Figure S6c). The origin of the larger split can be explained simply by looking at the pseudo-charge density, similarly to the parent compound $(Tz)_2PbBr_4$. Even though the structure is a $n = 1$ perovskite, to analyze interlayer interactions we consider the adjacent two layers next to Tz cation as a bilayer (Figure S8b). From Figure S8a, the split between the symmetry allowed optical transition of the bilayers in $(PA)(Tz)PbBr_4$ is just 55 meV, significantly smaller with respect to $(Tz)_2PbBr_4$. The second, even smaller split (~5 meV) is related to the lack of a mirror plane symmetry in the cell of $(PA)(Tz)PbBr_4$, which makes the two adjacent bilayers structurally non-equivalent. Thus, the pseudo-charge density in Figure S8b of the VBM and VBM-2, are projected on one of the bilayers in the unit cell, while the VBM-1 and VBM-3 are projected on the other. Therefore, there are four possible transitions in $(PA)(Tz)PbBr_4$ as shown in the calculated dielectric function of Figure S8a. These interactions are quantified in the effective masses (Table 5): for $(PA)_2PbBr_4$ the bands are found totally flat along the stacking direction. In contrast, for $(Tz)_2PbBr_4$ the effective masses in the stacking direction are much smaller ($<3\ m_e$). The effective masses of $(PA)(Tz)PbBr_4$, is in between the two parent compounds but still larger than 20 m_e, which can be considered as flat bands.

Conclusions

This study suggests that mixed-spacer 2D perovskites with different functional groups and special structures can lead to fine-tuned properties. The Tz cation can play a dual role in metal halide perovskite chemistry, as A-site cation in multilayer 2D perovskites (n>1) or spacer in mixed-spacer 2D n = 1 forming ordered superlattices with segregation of the spacers in different layers. The unique shape and size of Tz (larger compared to A-site cations such as MA, but smaller compared to linear ammonium spacer such as butylammonium) and ability to form multiple hydrogen bonds with the inorganic lattice as well as N-H$\cdots\pi$ interaction enables its impressive structural versatility. The multilayer 2D perovskites with large A-site cation series $(IPA)_2(Tz)_{n-1}Pb_nBr_{3n+1}$ (n = 1-3) are further stabilized by hydrogen bonding. Thanks to the strong hydrogen bonds, both the n = 2 and n = 3 phases form in this series. They exhibit small octahedral tilting (large Pb-Br-Pb angle) and large octahedral distortion (large distortion index). So far, the A-site cations that can fit into the halide perovskite cage include: cesium (Cs+), methylammonnium (MA), aziridinium (AzrH), formamidinium (FA), methylhydrazinium (MHy), 1,2,4-triazolinium (Tz), dimethylammonium (DMA), ethylammonium (EA), guanidinium (GA) and isopropylammonium (IPA) and some of them can also serve as spacers for the (100)-oriented 2D perovskites (e.g. MHy, Tz, EA and IPA). But Tz represents the rare case that it can serve as A cation (larger than MA) for both the n = 2 and n = 3 Pb perovskites.

The mixed-spacer phases $(PA)(Tz)PbBr_4$ and $(BA)(Tz)PbBr_4$ represent first cases of n = 1 structures with two distinct interlayer distances. The layers separated by Tz have a smaller interlayer distance than those separated by PA (and BA). These compounds are a clear example of how two different spacer cations and be accommodated in the same structure of 2D perovskites forming two distinct interlayer distances. First-principles calculations show that the interlayers of $(Tz)_2PbBr_4$ interact along the stacking axis, a rare feature for layered perovskites. Moreover, the electronic structure of $(PA)(Tz)PbBr_4$ combines the features of $(PA)_2PbBr_4$ and $(Tz)_2PbBr_4$, without being a simple composite with additive properties. Their optical properties are determined by the Pb-Br-Pb angles and distortion index of the structures. Either large tilting or large distortion can give rise to broad emission in $(IPA)_2(Tz)_{n-1}Pb_nBr_{3n+1}$ while the absence of both in $(PA)(Tz)PbBr_4$ leads to much narrower PL emission. We expect that organic cations with multiple N atoms can form strong hydrogen bonding and stabilize different structures beyond 2D

perovskites. Researchers have recently tried to combine the advantages of the Ruddlesden-Popper (RP) and Dion-Jacobson (DJ) phases for optoelectronic applications such as high performing solar cells.[13] However, it is challenging to determine the exact phase and structure on the spin-coated films. Our work suggests that it is possible to mix two spacers and form novel ordered mixed-spacer 2D perovskites. This work expands the structure types in 2D perovskites and suggests many possible combinations of spacer cations of potential interest for many kinds of optoelectronic devices.

ASSOCIATED CONTENT

Supporting Information

Starting materials, experimental details, crystallographic details, PXRD patterns and more optical properties.

X-ray crystallographic data of $(IPA)_2PbBr_4$.

X-ray crystallographic data of $(IPA)_2(Tz)Pb_2Br_7$.

X-ray crystallographic data of $(IPA)_2(Tz)_2Pb_3Br_{10}$.

X-ray crystallographic data of $(PA)(Tz)PbBr_4$.

X-ray crystallographic data of $(BA)(Tz)PbBr_4$.

X-ray crystallographic data of $(PA)_2PbBr_4$.

Author information

Corresponding Author

*m-kanatzidis@northwestern.edu

Notes

The authors declare no competing financial interest.

Acknowledgements

At Northwestern University, this work is mainly supported by the Office of Naval Research (ONR) under grant N00014-20-1-2725. Work at Yale is supported by the Yale University Lab Setup Fund. This work used the IMSERC facility at Northwestern University, which has received support from

the Soft and Hybrid Nanotechnology Experimental (SHyNE) Resource (NSF ECCS-2025633), and Northwestern University. At Rennes this work received funding from the Chaire de Recherche Rennes Metropole project and the European Union's Horizon 2020 research and innovation program under grant agreement No. 861985 (PeroCUBE). J.E. acknowledges financial support from the Institute Universitaire de France. This work was granted access to the HPC resources of TGCC under Allocations No. 2021-A0100911434 and 2021-A0110907682 made by GENCI. We acknowledge PRACE for awarding us access to ARCHER2, United Kingdom.

References

1. Saparov, B.; Mitzi, D. B., Organic–Inorganic Perovskites: Structural Versatility for Functional Materials Design. *Chem. Rev.* **2016,** *116* (7), 4558-4596.
2. Smith, M. D.; Crace, E. J.; Jaffe, A.; Karunadasa, H. I., The Diversity of Layered Halide Perovskites. *Annu. Rev. Mater. Res.* **2018,** *48* (1), 111-136.
3. Mao, L.; Stoumpos, C. C.; Kanatzidis, M. G., Two-Dimensional Hybrid Halide Perovskites: Principles and Promises. *J. Am. Chem. Soc.* **2019,** *141* (3), 1171-1190.
4. Katan, C.; Mercier, N.; Even, J., Quantum and Dielectric Confinement Effects in Lower-Dimensional Hybrid Perovskite Semiconductors. *Chem. Rev.* **2019,** *119* (5), 3140-3192.
5. Li, X.; Hoffman, J. M.; Kanatzidis, M. G., The 2D Halide Perovskite Rulebook: How the Spacer Influences Everything from the Structure to Optoelectronic Device Efficiency. *Chem. Rev.* **2021,** *121* (4), 2230-2291.
6. Stoumpos, C. C.; Cao, D. H.; Clark, D. J.; Young, J.; Rondinelli, J. M.; Jang, J. I.; Hupp, J. T.; Kanatzidis, M. G., Ruddlesden–Popper Hybrid Lead Iodide Perovskite 2D Homologous Semiconductors. *Chem. Mater.* **2016,** *28* (8), 2852-2867.
7. Mao, L.; Ke, W.; Pedesseau, L.; Wu, Y.; Katan, C.; Even, J.; Wasielewski, M. R.; Stoumpos, C. C.; Kanatzidis, M. G., Hybrid Dion–Jacobson 2D Lead Iodide Perovskites. *J. Am. Chem. Soc.* **2018,** *140* (10), 3775-3783.
8. Li, X.; Ke, W.; Traoré, B.; Guo, P.; Hadar, I.; Kepenekian, M.; Even, J.; Katan, C.; Stoumpos, C. C.; Schaller, R. D.; Kanatzidis, M. G., Two-Dimensional Dion–Jacobson Hybrid Lead Iodide Perovskites with Aromatic Diammonium Cations. *J. Am. Chem. Soc.* **2019,** *141* (32), 12880-12890.
9. Soe, C. M. M.; Stoumpos, C. C.; Kepenekian, M.; Traoré, B.; Tsai, H.; Nie, W.; Wang, B.; Katan, C.; Seshadri, R.; Mohite, A. D.; Even, J.; Marks, T. J.; Kanatzidis, M. G., New Type of 2D Perovskites with Alternating Cations in the Interlayer Space, $(C(NH_2)_3)(CH_3NH_3)_nPb_nI_{3n+1}$: Structure, Properties, and Photovoltaic Performance. *J. Am. Chem. Soc.* **2017,** *139* (45), 16297-16309.
10. Nazarenko, O.; Kotyrba, M. R.; Wörle, M.; Cuervo-Reyes, E.; Yakunin, S.; Kovalenko, M. V., Luminescent and Photoconductive Layered Lead Halide Perovskite Compounds Comprising Mixtures of Cesium and Guanidinium Cations. *Inorg. Chem.* **2017,** *56* (19), 11552-11564.
11. Daub, M.; Hillebrecht, H., From 1D to 3D: Perovskites within the System HSC(NH2)2I/CH3NH3I/PbI2 with Maintenance of the Cubic Closest Packing. *Inorg. Chem.* **2021,** *60* (5), 3082-3093.
12. Aubrey, M. L.; Saldivar Valdes, A.; Filip, M. R.; Connor, B. A.; Lindquist, K. P.; Neaton, J. B.; Karunadasa, H. I., Directed assembly of layered perovskite heterostructures as single crystals. *Nature* **2021,** *597* (7876), 355-359.
13. Fu, P.; Liu, Y.; Yu, S.; Yin, H.; Yang, B.; Ahmad, S.; Guo, X.; Li, C., Dion-Jacobson and Ruddlesden-Popper double-phase 2D perovskites for solar cells. *Nano Energy* **2021,** *88*, 106249.
14. Yan, L.; Jana, M. K.; Sercel, P. C.; Mitzi, D. B.; You, W., Alkyl–Aryl Cation Mixing in Chiral 2D Perovskites. *J. Am. Chem. Soc.* **2021,** *143* (43), 18114-18120.
15. Fu, Y.; Hautzinger, M. P.; Luo, Z.; Wang, F.; Pan, D.; Aristov, M. M.; Guzei, I. A.; Pan, A.; Zhu, X.; Jin, S., Incorporating Large A Cations into Lead Iodide Perovskite Cages: Relaxed Goldschmidt Tolerance Factor and Impact on Exciton–Phonon Interaction. *ACS Cent. Sci.* **2019,** *5* (8), 1377-1386.
16. Kieslich, G.; Sun, S.; Cheetham, A. K., Solid-state principles applied to organic–inorganic perovskites: new tricks for an old dog. *Chem. Sci.* **2014,** *5* (12), 4712-4715.
17. Kieslich, G.; Sun, S.; Cheetham, A. K., An extended Tolerance Factor approach for organic–inorganic perovskites. *Chem. Sci.* **2015,** *6* (6), 3430-3433.
18. Mączka, M.; Gagor, A.; Zaręba, J. K.; Stefanska, D.; Drozd, M.; Balciunas, S.; Šimėnas, M.; Banys, J.; Sieradzki, A., Three-Dimensional Perovskite Methylhydrazinium Lead Chloride with Two Polar Phases

and Unusual Second-Harmonic Generation Bistability above Room Temperature. *Chem. Mater.* **2020,** *32* (9), 4072-4082.
19. Mączka, M. a.; Ptak, M.; Gągor, A.; Stefańska, D.; Zaręba, J. K.; Sieradzki, A., Methylhydrazinium Lead Bromide: Noncentrosymmetric Three-Dimensional Perovskite with Exceptionally Large Framework Distortion and Green Photoluminescence. *Chem. Mater.* **2020,** *32* (4), 1667-1673.
20. Petrosova, H. R.; Kucheriv, O. I.; Shova, S.; Gural'skiy, I. y. A., Aziridinium cation templating 3D lead halide hybrid perovskites. *Chem. Commun.* **2022,** *58* (38), 5745-5748.
21. Li, X.; Cuthriell, S. A.; Bergonzoni, A.; Dong, H.; Traoré, B.; Stoumpos, C. C.; Guo, P.; Even, J.; Katan, C.; Schaller, R. D.; Kanatzidis, M. G., Expanding the Cage of 2D Bromide Perovskites by Large A-Site Cations. *Chem. Mater.* **2022,** *34* (3), 1132-1142.
22. Li, X.; Fu, Y.; Pedesseau, L.; Guo, P.; Cuthriell, S.; Hadar, I.; Even, J.; Katan, C.; Stoumpos, C. C.; Schaller, R. D.; Harel, E.; Kanatzidis, M. G., Negative Pressure Engineering with Large Cage Cations in 2D Halide Perovskites Causes Lattice Softening. *J. Am. Chem. Soc.* **2020,** *142* (26), 11486-11496.
23. Fu, Y.; Jiang, X.; Li, X.; Traore, B.; Spanopoulos, I.; Katan, C.; Even, J.; Kanatzidis, M. G.; Harel, E., Cation Engineering in Two-Dimensional Ruddlesden-Popper Lead Iodide Perovskites with Mixed Large A-Site Cations in the Cages. *J. Am. Chem. Soc.* **2020,** *142* (8), 4008-4021.
24. Han, S.; Liu, X.; Liu, Y.; Xu, Z.; Li, Y.; Hong, M.; Luo, J.; Sun, Z., High-Temperature Antiferroelectric of Lead Iodide Hybrid Perovskites. *J. Am. Chem. Soc.* **2019,** *141* (32), 12470-12474.
25. Mao, L.; Wu, Y.; Stoumpos, C. C.; Traore, B.; Katan, C.; Even, J.; Wasielewski, M. R.; Kanatzidis, M. G., Tunable White-Light Emission in Single-Cation-Templated Three-Layered 2D Perovskites $(CH_3CH_2NH_3)_4Pb_3Br_{10-x}Cl_x$. *J. Am. Chem. Soc.* **2017,** *139* (34), 11956-11963.
26. Stoumpos, C. C.; Mao, L.; Malliakas, C. D.; Kanatzidis, M. G., Structure–Band Gap Relationships in Hexagonal Polytypes and Low-Dimensional Structures of Hybrid Tin Iodide Perovskites. *Inorg. Chem.* **2017,** *56* (1), 56-73.
27. Kepenekian, M.; Traore, B.; Blancon, J.-C.; Pedesseau, L.; Tsai, H.; Nie, W.; Stoumpos, C. C.; Kanatzidis, M. G.; Even, J.; Mohite, A. D.; Tretiak, S.; Katan, C., Concept of Lattice Mismatch and Emergence of Surface States in Two-dimensional Hybrid Perovskite Quantum Wells. *Nano Lett.* **2018,** *18* (9), 5603-5609.
28. Paritmongkol, W.; Dahod, N. S.; Stollmann, A.; Mao, N.; Settens, C.; Zheng, S.-L.; Tisdale, W. A., Synthetic Variation and Structural Trends in Layered Two-Dimensional Alkylammonium Lead Halide Perovskites. *Chem. Mater.* **2019,** *31* (15), 5592.
29. Li, L.; Shang, X.; Wang, S.; Dong, N.; Ji, C.; Chen, X.; Zhao, S.; Wang, J.; Sun, Z.; Hong, M.; Luo, J., Bilayered Hybrid Perovskite Ferroelectric with Giant Two-Photon Absorption. *J. Am. Chem. Soc.* **2018,** *140* (22), 6806-6809.
30. Dohner, E. R.; Hoke, E. T.; Karunadasa, H. I., Self-Assembly of Broadband White-Light Emitters. *J. Am. Chem. Soc.* **2014,** *136* (5), 1718-1721.
31. Mao, L.; Wu, Y.; Stoumpos, C. C.; Wasielewski, M. R.; Kanatzidis, M. G., White-Light Emission and Structural Distortion in New Corrugated Two-Dimensional Lead Bromide Perovskites. *J. Am. Chem. Soc.* **2017,** *139* (14), 5210-5215.
32. Li, X.; Guo, P.; Kepenekian, M.; Hadar, I.; Katan, C.; Even, J.; Stoumpos, C. C.; Schaller, R. D.; Kanatzidis, M. G., Small Cyclic Diammonium Cation Templated (110)-Oriented 2D Halide (X = I, Br, Cl) Perovskites with White-Light Emission. *Chem. Mater.* **2019,** *31* (9), 3582-3590.
33. Daub, M.; Haber, C.; Hillebrecht, H., Synthesis, Crystal Structures, Optical Properties, and Phase Transitions of the Layered Guanidinium‐Based Hybrid Perovskites $[C(NH_2)_3]_2MI_4$; M = Sn, Pb. *Eur. J. Inorg. Chem.* **2016,** *2017* (7), 1120-1126.
34. Daub, M.; Hillebrecht, H., First representatives of (210)-oriented perovskite variants−Synthesis, crystal structures and properties of the new 2D hybrid perovskites $A[HC(NH_2)_2]PbI_4$; A=$[C(NH_2)_3]$, $[HSC(NH_2)_2]$. *Z. Kristallogr. - Cryst. Mater.* **2018,** *233* (8), 555.

35. Fateev, S. A.; Petrov, A. A.; Marchenko, E. I.; Zubavichus, Y. V.; Khrustalev, V. N.; Petrov, A. V.; Aksenov, S. M.; Goodilin, E. A.; Tarasov, A. B., FA2PbBr4: Synthesis, Structure, and Unusual Optical Properties of Two Polymorphs of Formamidinium-Based Layered (110) Hybrid Perovskite. *Chem. Mater.* **2021,** *33* (5), 1900-1907.
36. Guo, Y.-Y.; Yang, L.-J.; Biberger, S.; McNulty, J. A.; Li, T.; Schötz, K.; Panzer, F.; Lightfoot, P., Structural Diversity in Layered Hybrid Perovskites, A_2PbBr_4 or $AA'PbBr_4$, Templated by Small Disc-Shaped Amines. *Inorg. Chem.* **2020,** *59* (17), 12858-12866.
37. Mączka, M.; Ptak, M.; Gągor, A.; Stefańska, D.; Sieradzki, A., Layered Lead Iodide of [Methylhydrazinium]2PbI4 with a Reduced Band Gap: Thermochromic Luminescence and Switchable Dielectric Properties Triggered by Structural Phase Transitions. *Chem. Mater.* **2019,** *31* (20), 8563-8575.
38. Mączka, M.; Zaręba, J. K.; Gągor, A.; Stefańska, D.; Ptak, M.; Roleder, K.; Kajewski, D.; Soszyński, A.; Fedoruk, K.; Sieradzki, A., [Methylhydrazinium]2PbBr4, a Ferroelectric Hybrid Organic–Inorganic Perovskite with Multiple Nonlinear Optical Outputs. *Chem. Mater.* **2021,** *33* (7), 2331-2342.
39. McNulty, J. A.; Lightfoot, P., Unprecedented tin iodide perovskite-like structures featuring ordering of organic moieties. *Chem. Commun.* **2020,** *56*, 4543-4546.
40. Smith, M. D.; Jaffe, A.; Dohner, E. R.; Lindenberg, A. M.; Karunadasa, H. I., Structural origins of broadband emission from layered Pb-Br hybrid perovskites. *Chem. Sci.* **2017,** *8* (6), 4497-4504.
41. Li, X.; Hoffman, J.; Ke, W.; Chen, M.; Tsai, H.; Nie, W.; Mohite, A. D.; Kepenekian, M.; Katan, C.; Even, J.; Wasielewski, M. R.; Stoumpos, C. C.; Kanatzidis, M. G., Two-Dimensional Halide Perovskites Incorporating Straight Chain Symmetric Diammonium Ions, $(NH_3C_mH_{2m}NH_3)(CH_3NH_3)_{n-1}Pb_nI_{3n+1}$ (m = 4–9; n = 1–4). *J. Am. Chem. Soc.* **2018,** *140* (38), 12226-12238.
42. Hückel, E., Quantentheoretische Beiträge zum Benzolproblem. *Zeitschrift für Physik* **1931,** *70* (3), 204-286.
43. Mitzi, D. B.; Brock, P., Structure and Optical Properties of Several Organic−Inorganic Hybrids Containing Corner-Sharing Chains of Bismuth Iodide Octahedra. *Inorg. Chem.* **2001,** *40* (9), 2096-2104.
44. Pedesseau, L.; Sapori, D.; Traore, B.; Robles, R.; Fang, H.-H.; Loi, M. A.; Tsai, H.; Nie, W.; Blancon, J.-C.; Neukirch, A.; Tretiak, S.; Mohite, A. D.; Katan, C.; Even, J.; Kepenekian, M., Advances and Promises of Layered Halide Hybrid Perovskite Semiconductors. *ACS Nano* **2016,** *10* (11), 9776-9786.
45. Robinson, K.; Gibbs, G. V.; Ribbe, P. H., Quadratic Elongation: A Quantitative Measure of Distortion in Coordination Polyhedra. *Science* **1971,** *172* (3983), 567-570.
46. Momma, K.; Izumi, F., VESTA 3 for three-dimensional visualization of crystal, volumetric and morphology data. *J. Appl. Crystallogr.* **2011,** *44* (6), 1272-1276.
47. Janiak, C., A critical account on π–π stacking in metal complexes with aromatic nitrogen-containing ligands. *J. Chem. Soc., Dalton Trans.* **2000,** (21), 3885-3896.
48. Xu, Z.; Mitzi, D. B., SnI42--Based Hybrid Perovskites Templated by Multiple Organic Cations: Combining Organic Functionalities through Noncovalent Interactions. *Chem. Mater.* **2003,** *15* (19), 3632-3637.
49. Mao, L.; Guo, P.; Kepenekian, M.; Spanopoulos, I.; He, Y.; Katan, C.; Even, J.; Schaller, R. D.; Seshadri, R.; Stoumpos, C. C.; Kanatzidis, M. G., Organic Cation Alloying on Intralayer A and Interlayer A' sites in 2D Hybrid Dion-Jacobson Lead Bromide Perovskites (A')(A)Pb_2Br_7. *J. Am. Chem. Soc.* **2020,** *142* (18), 8342-8351.
50. Mitzi, D. B.; Medeiros, D. R.; Malenfant, P. R. L., Intercalated Organic−Inorganic Perovskites Stabilized by Fluoroaryl−Aryl Interactions. *Inorg. Chem.* **2002,** *41* (8), 2134-2145.
51. Li, L.; Sun, Z.; Wang, P.; Hu, W.; Wang, S.; Ji, C.; Hong, M.; Luo, J., Tailored Engineering of an Unusual $(C_4H_9NH_3)_2(CH_3NH_3)_2Pb_3Br_{10}$ Two-Dimensional Multilayered Perovskite Ferroelectric for a High-Performance Photodetector. *Angew. Chem., Int. Ed.* **2017,** *56* (40), 12150-12154.

52. Li, L.; Liu, X.; Li, Y.; Xu, Z.; Wu, Z.; Han, S.; Tao, K.; Hong, M.; Luo, J.; Sun, Z., Two-Dimensional Hybrid Perovskite-Type Ferroelectric for Highly Polarization-Sensitive Shortwave Photodetection. *J. Am. Chem. Soc.* **2019,** *141* (6), 2623-2629.
53. Li, X.; He, Y.; Kepenekian, M.; Guo, P.; Ke, W.; Even, J.; Katan, C.; Stoumpos, C. C.; Schaller, R. D.; Kanatzidis, M. G., Three-dimensional Lead Iodide Perovskitoid Hybrids with High X-ray Photoresponse. *J. Am. Chem. Soc.* **2020,** *142* (14), 6625-6637.
54. Quarti, C.; Grancini, G.; Mosconi, E.; Bruno, P.; Ball, J. M.; Lee, M. M.; Snaith, H. J.; Petrozza, A.; De Angelis, F., The Raman Spectrum of the $CH_3NH_3PbI_3$ Hybrid Perovskite: Interplay of Theory and Experiment. *J. Phys. Chem. Lett.* **2014,** *5* (2), 279-284.
55. Yaffe, O.; Guo, Y.; Tan, L. Z.; Egger, D. A.; Hull, T.; Stoumpos, C. C.; Zheng, F.; Heinz, T. F.; Kronik, L.; Kanatzidis, M. G.; Owen, J. S.; Rappe, A. M.; Pimenta, M. A.; Brus, L. E., Local Polar Fluctuations in Lead Halide Perovskite Crystals. *Phys. Rev. Lett.* **2017,** *118* (13), 136001.
56. Febriansyah, B.; Borzda, T.; Cortecchia, D.; Neutzner, S.; Folpini, G.; Koh, T. M.; Li, Y.; Mathews, N.; Petrozza, A.; England, J., Metal Coordination Sphere Deformation Induced Highly Stokes-Shifted, Ultra Broadband Emission in 2D Hybrid Lead-Bromide Perovskites and Investigation of Its Origin. *Angew. Chem., Int. Ed.* **2020,** *59* (27), 10791-10796.

Table 1. Crystal and Refinement Data for $(IPA)_2(Tz)_{n-1}Pb_nBr_{3n+1}$ (n = 1–3) series at Room Temperature.

Empirical formula	$(IPA)_2PbBr_4$	$(IPA)_2(Tz)Pb_2Br_7$	$(IPA)_2(Tz)_2Pb_3Br_{10}$
Crystal system	monoclinic	monoclinic	monoclinic
Space group	*Cc*	*C*2	$P2_1$
Unit cell dimensions	*a* = 23.400(6) Å *b* = 8.344(2) Å *c* = 8.452(2) Å *β* = 90.139(13)°	*a* = 35.2952(12) Å *b* = 6.0342(2) Å *c* = 6.0327(2) Å *β* = 99.834(3)°	*a* = 8.5126(4) Å *b* = 8.5069(4) Å *c* = 23.8070(11) Å *β* = 96.965(3)°
Volume	1650.4(7) $Å^3$	1265.96(7) $Å^3$	1711.28(14) $Å^3$
Z	4	2	2
Density (calculated)	2.6042 g/cm^3	3.0537 g/cm^3	3.2623 g/cm^3
Index ranges	-32<=h<=32 -11<=k<=11 -11<=l<=12	-49<=h<=49 -8<=k<=8 -8<=l<=8	-12<=h<=11 -11<=k<=11 -33<=l<=33
Independent reflections	2946 [R_{int} = 0.0454]	2288 [R_{int} = 0.0406]	9992 [R_{int} = 0.0555]
Completeness to θ = 25°	98%	100%	100%
Data / restraints / parameters	2946 / 12 / 73	2288 / 13 / 64	9992 / 33 / 179
Goodness-of-fit	2.64	4.47	2.80
Final R indices [I>2σ(I)]	R_{obs} = 0.0456 wR_{obs} = 0.0580	R_{obs} = 0.0552 wR_{obs} = 0.0843	R_{obs} = 0.0703 wR_{obs} = 0.0919
R indices [all data]	R_{all} = 0.0589 wR_{all} = 0.0623	R_{all} = 0.0614 wR_{all} = 0.0848	R_{all} = 0.0781 wR_{all} = 0.0924
Largest diff. peak and hole	1.94 and -1.82 $e·Å^{-3}$	1.91 and -2.25 $e·Å^{-3}$	3.63 and -3.64 $e·Å^{-3}$

Table 2. Comparison of Distortion Index and Bond Angle Variance.

	Distortion index	Bond angle variance
$(IPA)PbBr_4$	0.014	1.2
$(IPA)_2(Tz)Pb_2Br_7$	0.031	2.8
$(IPA)_2(Tz)_2Pb_3Br_{10}$	0.027	65.0
$(PA)(Tz)PbBr_4$	0.011	18.9
$(BA)(Tz)PbBr_4$	0.011	20.4
$(PA)_2PbBr_4$	0.002	8.0
$(BA)_2PbBr_4$	0.002	9.4
$(Tz)_2PbBr_4$	0.004	33.6

Table 3. Crystal and Refinement Data for the (PA)(Tz)$PbBr_4$ and (BA)(Tz)$PbBr_4$ at Room Temperature.

Empirical formula	(PA)(Tz)$PbBr_4$	(BA)(Tz)$PbBr_4$
Crystal system	monoclinic	monoclinic
Space group	$P2_1/c$	$P2_1/c$
Unit cell dimensions	a = 44.1330(13) Å b = 8.4225(2) Å c = 8.3101(2) Å β = 90.0019(16)°	a = 46.5492(12) Å b = 8.4342(2) Å c = 8.3087(2) Å β = 90.0022(14)°
Volume	3088.95(14) $Å^3$	3262.04(14) $Å^3$
Z	8	8
Density (calculated)	2.826 g/cm^3	2.733 g/cm^3
Index ranges	-62<=h<=62, -11<=k<=11, -11<=l<=11	-65<=h<=65, -11<=k<=11, -11<=l<=11
Independent reflections	9070 [R_{int} = 0.0474]	9705 [R_{int} = 0.0488]
Completeness to θ = 25°	99.9%	99.9%
Data / restraints / parameters	9070 / 12 / 153	9705 / 19 / 159
Goodness-of-fit	1.226	1.401
Final R indices [I > 2σ(I)]	R_{obs} = 0.0660, wR_{obs} = 0.1740	R_{obs} = 0.0612, wR_{obs} = 0.1460
R indices [all data]	R_{all} = 0.0847, wR_{all} = 0.1824	R_{all} = 0.0713, wR_{all} = 0.1558
Largest diff. peak and hole	1.809 and -3.136 $e·Å^{-3}$	1.660 and -3.362 $e·Å^{-3}$

Table 4. Comparison of Average Pb-Br-Pb Angles and Experimental Optical Bandgaps.

	Pb-Br-Pb (°)	Bandgap (eV)
(PA)(Tz)$PbBr_4$	161.2	2.79
$(PA)_2PbBr_4$	153.8	2.89
$(Tz)_2PbBr_4$	166.0	2.71
(BA)(Tz)$PbBr_4$	161.1	2.77
$(BA)_2PbBr_4$	154.8	2.88

Table 5. Effective Masses (m_0) of Electrons (m_e) and Holes (m_h) for $(PA)_2PbBr_4$, $(Tz)_2PbBr_4$ and $(PA)(Tz)PbBr_4$. (The ±1, ±2, ±3 indicates the different bands as shown in Figure S7a and S8a. The bands are labeled as flat when $m > 20m_e$.)

Compound		x	y	z (long axis)
$(PA)_2PbBr_4$	m_e	0.22	0.22	flat
	m_h	0.27	0.27	flat
		x	y	z (long axis)
$(Tz)_2PbBr_4$	m_e+1	0.17	0.14	-3.0
	m_e	0.19	0.28	2.7
	m_h	0.24	0.25	1.7
	m_h-1	0.23	0.22	-2.5
		x (long axis)	y	z
$(PA)(Tz)PbBr_4$	m_e+3	flat	0.11	0.19
	m_e+2	flat	0.12	0.19
	m_e+1	flat	0.69	0.20
	m_e	flat	0.59	0.20
	m_h	flat	0.28	0.25
	m_h-1	flat	0.28	0.24
	m_h-2	flat	0.22	0.23
	m_h-3	flat	0.21	0.23

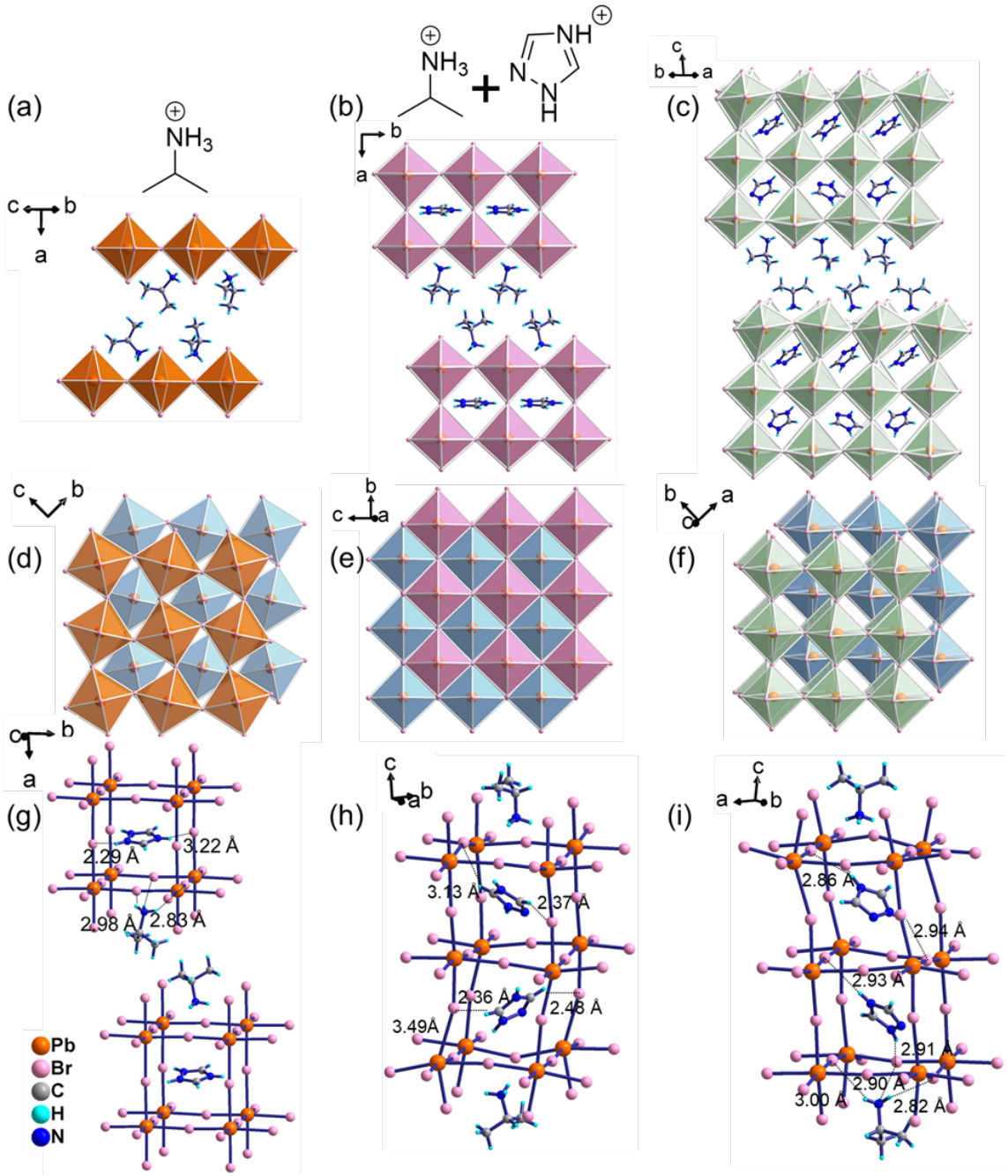

Figure 1. Crystal structures of the $(IPA)_2(Tz)_{n-1}Pb_nBr_{3n+1}$ (n = 1–3) series. Side view of (a) n = 1, (b) n = 2 and (c) n = 3. Top view of (d) n = 1, (e) n = 2 and (f) n = 3. Crystal structures of (g) n = 2 and (h)(i) n = 3 emphasizing the perovskite cages. The dash lines in (g)(h)(i) indicate the hydrogen bonds.

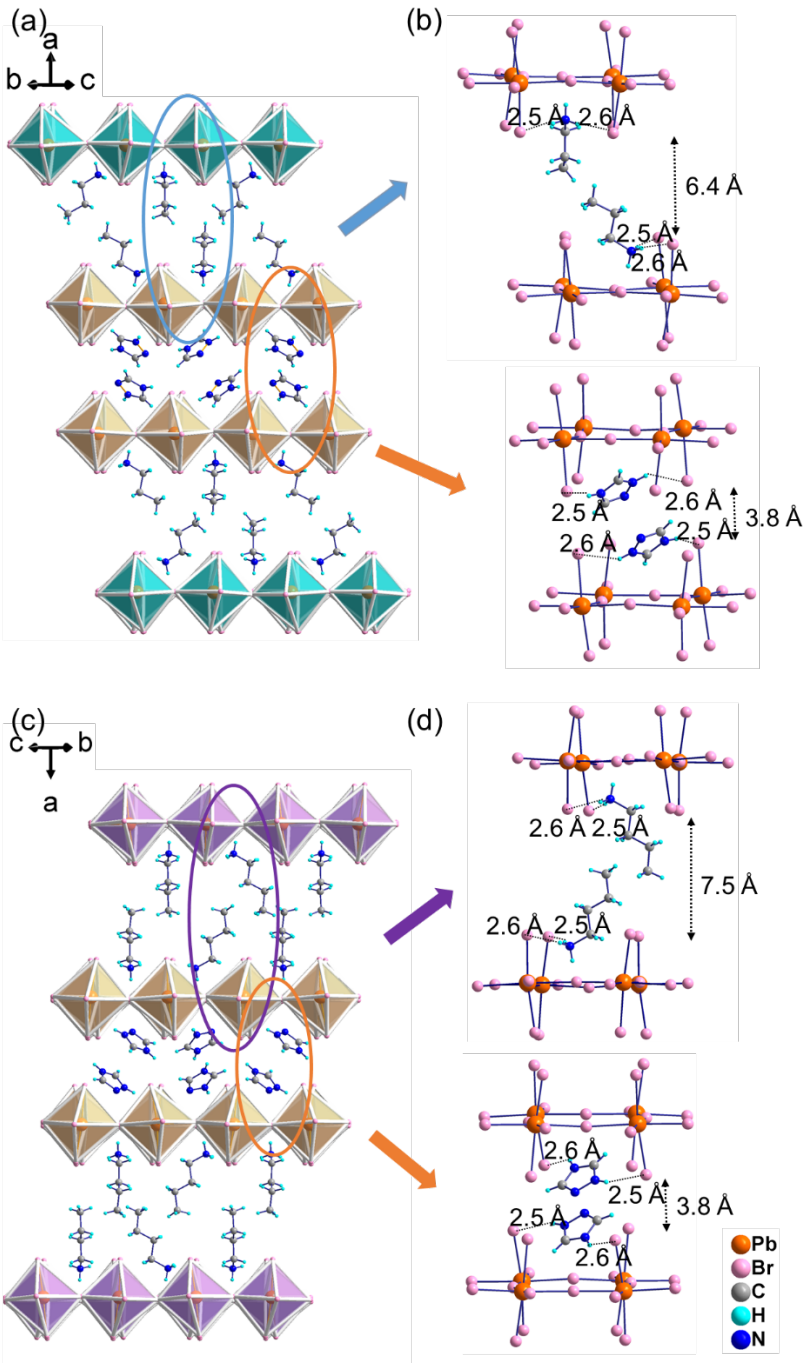

Figure 2. Crystal structures of (a)(b) (PA)(Tz)$PbBr_4$ and (c)(d) (BA)(Tz)$PbBr_4$. The dash lines in (b)(d) indicate the hydrogen bonds.

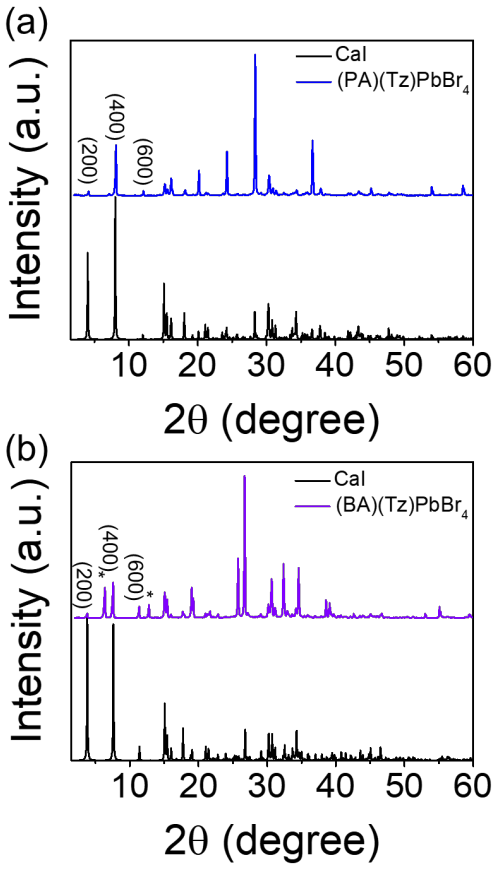

Figure 3. PXRD patterns of (a) $(PA)(Tz)PbBr_4$ and (b) $(BA)(Tz)PbBr_4$. The asterisks indicate the $(BA)_2PbBr_4$ phase.

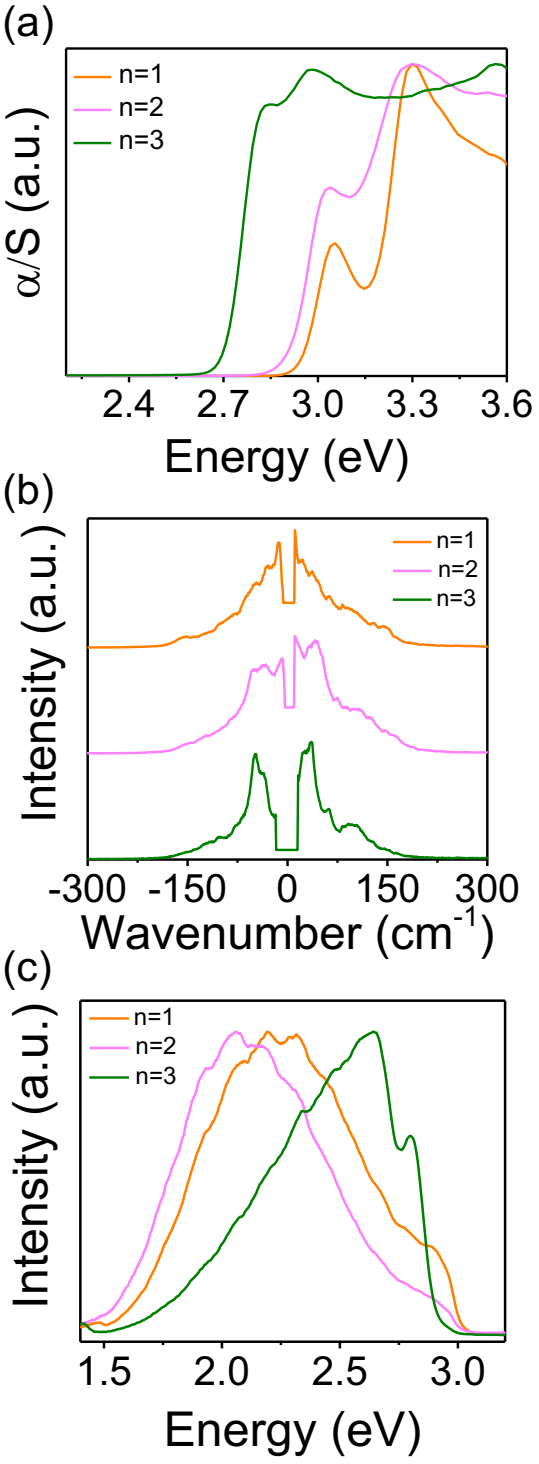

Figure 4. (a) Absorption spectra, (b) low-frequency Raman spectra and (c) integrated PL spectra at room temperature for the $(IPA)_2(Tz)_{n-1}Pb_nBr_{3n+1}$ (n = 1–3) series.

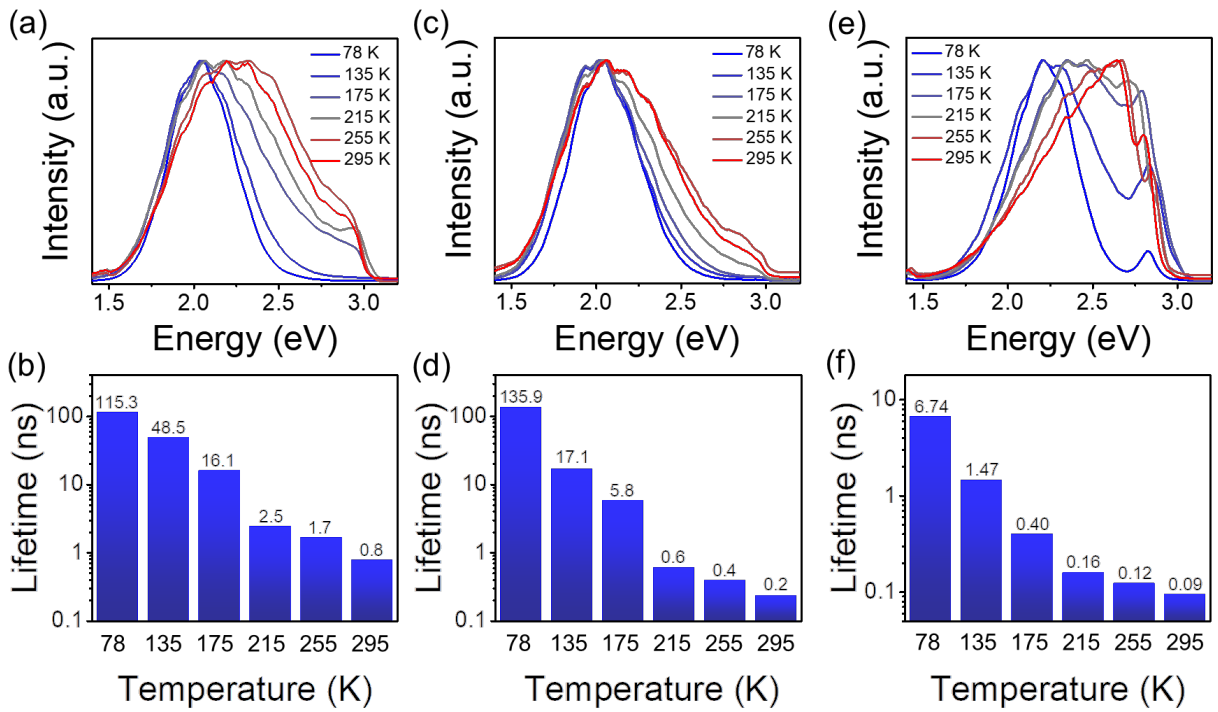

Figure 5. Normalized temperature-dependent PL spectra and corresponding PL lifetimes for the $(IPA)_2(Tz)_{n-1}Pb_nBr_{3n+1}$ (n = 1–3) series. (a)(b) n = 1, (c)(d) n = 2 and (e)(f) n = 3.

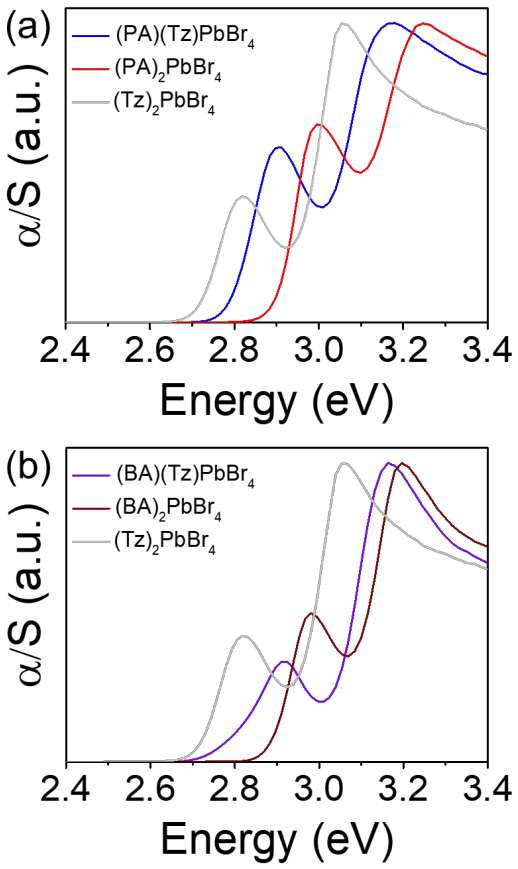

Figure 6. Absorption spectra of (a) $(PA)(Tz)PbBr_4$ and (b) $(BA)(Tz)PbBr_4$, compared to their parent compounds.

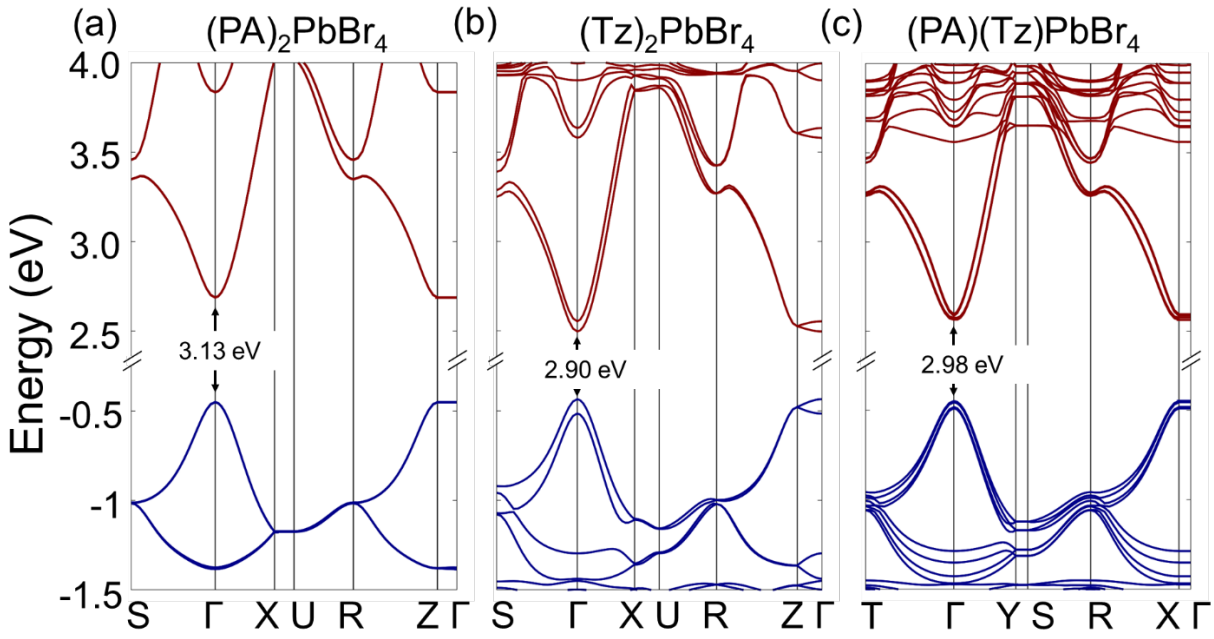

Figure 7. Electronic band structures of (a) $(PA)_2PbBr_4$, (b) $(Tz)_2PbBr_4$ and (c) $(PA)(Tz)PbBr_4$. The bandgaps reported are calculated by employing the PBE0 hybrid functional.

TOC graphic

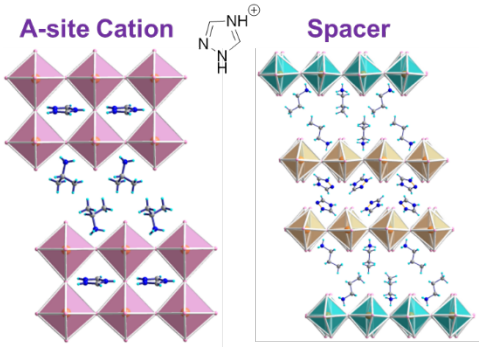

Chemistry of Materials DOI: 10.1021/acs.chemmater.2c01432

Supporting Information

Ordered Mixed-spacer 2D Bromide Perovskites and The Dual Role of 1,2,4-triazolium Cation

Xiaotong Li,[†] Hao Dong,[‡] George Volonakis,[§] Constantinos C. Stoumpos,[▽] Jacky Even,[‖] Claudine Katan,[§] Peijun Guo,[‡] and Mercouri G. Kanatzidis[*,†]

[†]Department of Chemistry, Northwestern University, Evanston, Illinois 60208, United States
[‡]Department of Chemical and Environmental Engineering, Yale University, New Haven, Connecticut 06511, United States
[§]Univ Rennes, ENSCR, INSA Rennes, CNRS, ISCR (Institut des Sciences Chimiques de Rennes), UMR 6226, Rennes F-35000, France
[‖]Univ Rennes, INSA Rennes, CNRS, Institut FOTON, UMR 6082, Rennes F-35000, France
[▽]Department of Materials Science and Technology, Voutes Campus, University of Crete, Heraklion GR-70013, Greece

Powder X-ray Diffraction. Powder X-ray diffraction analysis was performed using a Rigaku Miniflex600 powder X-ray diffractometer (Cu Kα graphite, λ = 1.5406 Å) operating at 40 kV/15 mA with a Kβ foil filter.

Single-Crystal X-ray Diffraction. The compounds were collected either using a Bruker DUO or Molly instrument with a Mo Kα IμS microfocus source (λ = 0.71073 Å) with MX Optics at 298 K for all three compounds and at 250 K for the bromide compound. The collected data were integrated and applied with numerical absorption corrections using the APEX3 software.

Optical Absorption Spectroscopy. Optical diffuse reflectance measurements were performed using a Shimadzu UV-3600 UV−vis NIR spectrometer operating in the 200−2500 nm region at room temperature. $BaSO_4$ was used as the reference of 100% reflectance for all measurements. The reflectance versus wavelength data generated was used to estimate the bandgap of the material by converting reflectance to absorption data according to the Kubelka−Munk equation: $\alpha/S = (1-R)^2(2R)^{-1}$, where R is the reflectance and α and S are the absorption and scattering coefficients, respectively.

Photoluminescence. Photoluminescence was measured using a 375 nm ps laser (Picoquant LDH-D-C-375) as the excitation source running at a 10 MHz repetition rate. A long-working-distance objective (Mitutoyo, 10X, NA=0.28) was used to focus the laser onto the samples and collect the PL signal. The samples were mounted in a liquid-nitrogen cryostat (Janis VPF-100) at a pressure below 10^{-4} Torr. A dichroic mirror was placed on the path to block the reflected laser light, and a 400 nm long-pass filter was placed near the entrance slit of the spectrograph (Andor Kymera 328i) to further reject any residual laser light. Time-integrated PL spectra were captured by a Si EMCCD (Andor iXon Life 888), and time-resolved PL was collected by a streak camera (Hamamatsu C10910 with the Slow sweep unit; M10913).

Raman Spectra. Low-frequency Raman spectra were measured using a frequency-stabilized 785 nm laser (Toptica) as the excitation source with an incident power of 40 mW onto the sample. A set of 5 narrow-linewidth notch filters (OptiGrate) was used to reject the laser line and enable measurements of Raman signatures down to 5 cm^{-1}. A super-long-working-distance objective lens (10X, NA=0.28) was used to focus the excitation light and collect the Raman signal. The Raman signal was spatially filtered by a pair of 75-mm achromatic lenses and a 50-μm pinhole before sent

into the spectrograph (Andor Kymera 328i). The Raman signal was finally captured by a Si EMCCD (Andor iXon Life 888).

Computational details. All first-principles calculations were performed within the density functional theory (DFT) employing the codes VASP[1], the Quantum Espresso suite[2] (QE) and the YAMBO code[3]. The experimental structures (i.e., lattice parameters and atomic coordinates) were used to model the compounds. C-H and N-H bond lengths were fixed to the standard values (1.089 Å and 1.015 Å, respectively). The band structures were calculated employing VASP and the projected augmented waves method[4] and the Perdew-Burke-Erzenhoff[5] (PBE) exchange correlation functional. The kinetic energy cut-off for the plane-waves was set at 400 eV, the electronic convergence at 10^{-7}eV. We employed a 4x4x2 and 1x4x4 uniform Γ-centered k-point grid for the parent [$(PA)_2PbBr_4$, $(BA)_2PbBr_4$, $(Tz)_2PbBr_4$] and the mixed spacer compounds [$(PA)(Tz)PbBr_4$, $(BA)(Tz)PbBr_4$], respectively. For the $(IPA)_2(Tz)_{n-1}Pb_nBr_{3n+1}$ (n = 1-3) series we employed k-grids of 4x4x4 and 2x2x2 for the n=1,2 and n=3, respectively. All calculations take into account spin-orbit coupling (SOC) interactions. For the hybrid functional calculations (which give more accurate values for the calculated bandgaps, but the trend is the same), we used the PBE0[6] (i.e., $\alpha = 0.25$) as implemented in VASP, we employed a uniform 2x2x1 (or 1x2x2 depending on the direction of the long axis) uniform Γ-centered k-point grid. In the manuscript, we rigidly shift the electronic band structures to match the PBE0 calculated bandgap of each material. For the symmetry analysis, fat-bands, the plots of the squared pseudo-wavefunctions, and the dielectric function plots, we employed QE and YAMBO, using standard norm-conserving PBE pseudo-potentials from pseudo-dojo[7], with a cut-off set at 100 Ry. To get the sign of the squared pseudo-wavefunctions and show the bonding/anti-bonding character of the interlayer interactions, we performed a calculation without SOC, and looked only at the valence band top states, which are not significantly affected by SOC. The effective mass tensor was calculated using first-order finite differences, with a displacement of 0.01 in (2π/a) units, with the lattice constant of each compound.

Table S1. Comparison of Pb-Br-Pb Angles (°) for the $(IPA)_2(Tz)_{n-1}Pb_nBr_{3n+1}$ (n = 1-3) series (The red ones are the axial Pb-Br-Pb angles).

$(IPA)_2PbBr_4$		**$(IPA)_2(Tz)_2Pb_3Br_{10}$**	
Pb(1)-Br(1)-Pb(1)#3	155.35(15)	Pb(1)-Br(6)-Pb(1)#3	174.42(12)
Pb(1)-Br(2)-Pb(1)#5	153.78(16)	Pb(1)-Br(8)-Pb(1)#9	174.36(13)
Ave eq angle	154.57(16)	Pb(2)#10-Br(4)-Pb(3)	156.34(11)
		Pb(2)-Br(7)-Pb(3)	172.43(12)
		Pb(2)-Br(9)-Pb(3)#5	174.30(16)
$(IPA)_2(Tz)Pb_2Br_7$		Pb(2)-Br(1)-Pb(3)#4	171.06(16)
Pb(1)#6-Br(3)-Pb(1)	175.8(2)	Pb(1)-Br(10)-Pb(2)	171.67(12)
Pb(1)-Br(5)-Pb(1)#3	176.54(9)	Pb(1)-Br(5)-Pb(3)	164.82(12)
Pb(1)-Br(1)-Pb(1)#7	178.6(4)	Ave eq Pb-Br-Pb	170.49(13)
Ave eq Pb-Br-Pb	176.17(15)	Ave ax Pb-Br-Pb	168.25(12)
Ave Pb-Br-Pb	176.98(23)	Ave Pb-Br-Pb	169.93(13)

Table S2. Comparison of Pb-Br Bond Lengths (Å) for the $(IPA)_2(Tz)_{n-1}Pb_nBr_{3n+1}$ (n = 1-3) series.

$(IPA)_2PbBr_4$		**$(IPA)_2(Tz)_2Pb_3Br_{10}$**	
Pb(1)-Br(1)	3.016(5)	Pb(1)-Br(6)	3.001(3)
Pb(1)-Br(1)#1	3.043(4)	Pb(1)-Br(6)#1	3.047(3)
Pb(1)-Br(2)	3.070(5)	Pb(1)-Br(8)	2.978(3)
Pb(1)-Br(2)#2	3.047(4)	Pb(1)-Br(8)#2	3.066(3)
Pb(1)-Br(3)	2.965(5)	Pb(2)-Br(7)	2.972(3)
Pb(1)-Br(4)	2.940(6)	Pb(2)-Br(9)	2.999(4)
Ave eq Pb-Br	3.044(5)	Pb(2)-Br(1)	3.017(4)
Ave ax Pb-Br	2.953(6)	Pb(2)-Br(4)#6	3.077(3)
Ave Pb-Br	3.014(5)	Pb(3)-Br(7)	3.108(3)
		Pb(3)-Br(9)#7	3.025(4)
		Pb(3)-Br(1)#8	3.026(3)
$(IPA)_2(Tz)Pb_2Br_7$		Pb(3)-Br(4)	3.026(3)
Pb(1)-Br(3)	3.0205(16)	Pb(2)-Br(10)	3.110(3)
Pb(1)-Br(3)#1	3.0163(16)	Pb(3)-Br(5)	3.496(2)
Pb(1)-Br(5)#2	2.956(9)	Pb(1)-Br(5)	3.007(2)
Pb(1)-Br(5)	3.081(9)	Pb(1)-Br(10)	3.031(3)
Pb(1)-Br(2)	2.784(3)	Pb(2)-Br(2)	2.835(3)
Pb(1)-Br(1)	3.1869(6)	Pb(3)-Br(3)	2.774(3)
Ave eq Pb-Br	3.018(5)	Ave eq Pb-Br	3.028(3)
Ave ax Pb-Br	2.985(2)	Ave ax Pb-Br	3.042(3)
Ave Pb-Br	3.007(4)	Ave Pb-Br	3.033(3)

Table S3. Crystal data and structure refinement for $(PA)_2PbBr4$ at 293 K.

Empirical formula	C6 H20 Br4 N2 Pb1
Crystal system	orthorhombic
Space group	*Pbca*
Unit cell dimensions	*a* = 8.2949(9) Å *b* = 8.2137(7) Å *c* = 25.152(3) Å
Volume	1713.6(3) $Å^3$
Z	4
Density (calculated)	2.508 g/cm^3
Index ranges	-11<=h<=11, -11<=k<=11, -34<=l<=34
Independent reflections	1540 [R_{int} = 0.0521]
Completeness to θ = 25°	100%
Data / restraints / parameters	1540 / 5 / 38
Goodness-of-fit	2.17
Final R indices [I>2σ(I)]	R_{obs} = 0.0492, wR_{obs} = 0.0417
R indices [all data]	R_{all} = 0.0648, wR_{all} = 0.0434
Largest diff. peak and hole	1.06 and -1.55 $e \cdot Å^{-3}$

Table S4. Comparison of distortion index ($D = \frac{1}{6}\sum_i^6 \frac{|l_i - l_{av}|}{l_{av}}$), bond angle variance ($\sigma^2 = \sum_{i=1}^{12}(\theta_i - 90)^2/11$), average Pb-Br bond length and average Pb-Br-Pb angle.

	Distortion index	Bond angle variance	Ave Pb-Br (Å)	Ave Pb-Br-Pb (°)
$(IPA)_2(Tz)Pb_2Br_7$	0.031	2.8	3.01	176.98
$(IPA)_2(Tz)_2Pb_3Br_{10}$	0.027	65.0	3.03	169.93
$(BA)_2(MA)Pb_2Br_7$	0.011	20.1	2.99	160.37
$(BA)_2(MA)_2Pb_3Br_{10}$	0.013	9.5	2.99	166.48

Table S5. Atomic coordinates ($x10^4$) and equivalent isotropic displacement parameters ($Å^2x10^3$) for $(IPA)_2PbBr_4$ at 293 K with estimated standard deviations in parentheses.

Label	x	y	z	Occupancy	U_{eq}^*
Pb(1)	2801(1)	2516(2)	4591(2)	1	47(1)
Br(1)	2805(2)	4435(4)	1567(5)	1	55(2)
Br(2)	2805(2)	580(4)	7679(5)	1	60(2)
Br(3)	1534(2)	2446(7)	4523(8)	1	146(4)
Br(4)	4057(2)	2456(7)	4527(9)	1	144(4)

Table S6. Anisotropic displacement parameters ($Å^2x10^3$) for $(IPA)_2PbBr_4$ at 293 K with estimated standard deviations in parentheses.

Label	U_{11}	U_{22}	U_{33}	U_{12}	U_{13}	U_{23}
Pb(1)	51(1)	43(1)	46(1)	0(1)	0(1)	1(1)
Br(1)	60(2)	52(3)	54(3)	1(2)	0(2)	18(2)
Br(2)	80(3)	50(3)	50(2)	-1(2)	0(2)	15(2)
Br(3)	45(3)	248(10)	145(6)	28(3)	23(3)	70(4)
Br(4)	62(3)	232(10)	136(5)	-28(3)	-24(3)	59(3)

Table S7. Atomic coordinates ($x10^4$) and equivalent isotropic displacement parameters ($Å^2x10^3$) for $(IPA)_2(Tz)Pb_2Br_7$ at 293 K with estimated standard deviations in parentheses.

Label	x	y	z	Occupancy	U_{eq}^*
Pb(1)	5916(1)	3717(4)	914(1)	1	64(1)
Br(1)	5000	3652(19)	0	1	122(2)
Br(2)	6717(1)	3690(20)	1709(11)	1	274(3)
Br(3)	5940(1)	3596(15)	-4065(2)	1	102(1)
Br(5)	5942(1)	8821(15)	935(3)	1	102(1)

Table S8. Anisotropic displacement parameters ($Å^2x10^3$) for $(IPA)_2(Tz)Pb_2Br_7$ at 293 K with estimated standard deviations in parentheses.

Label	U_{11}	U_{22}	U_{33}	U_{12}	U_{13}	U_{23}
Pb(1)	76(1)	59(1)	56(1)	-11(1)	14(1)	-4(1)
Br(1)	81(2)	143(3)	142(3)	0	16(2)	0
Br(2)	66(2)	375(7)	372(6)	-1(7)	10(3)	35(9)
Br(3)	178(2)	87(2)	46(1)	9(2)	31(1)	7(2)
Br(5)	178(2)	40(2)	92(2)	-2(2)	30(2)	2(2)

Table S9. Atomic coordinates ($x10^4$) and equivalent isotropic displacement parameters ($Å^2x10^3$) for $(IPA)_2(Tz)_2Pb_3Br_{10}$ at 293 K with estimated standard deviations in parentheses.

Label	x	y	z	Occupancy	U_{eq}^*
Pb(1)	7534(1)	2675(1)	107(1)	1	32(1)
Pb(2)	9236(1)	1828(1)	2663(1)	1	36(1)
Pb(3)	14244(1)	-3214(2)	2584(1)	1	45(1)
Br(1)	6679(4)	-606(4)	2713(2)	1	83(2)
Br(2)	10159(4)	1404(5)	3838(2)	1	119(2)
Br(3)	14123(4)	-2862(5)	3737(2)	1	110(2)
Br(4)	16802(4)	-5645(3)	2888(2)	1	72(2)
Br(5)	7068(2)	2599(3)	-1165(1)	1	47(1)
Br(6)	9879(4)	123(3)	-47(2)	1	56(1)
Br(7)	11648(4)	-633(3)	2540(2)	1	61(1)
Br(8)	5069(4)	180(3)	63(2)	1	63(1)
Br(9)	11641(5)	4402(4)	2660(2)	1	85(2)
Br(10)	8548(4)	2071(4)	1353(1)	1	86(2)

Table S10. Anisotropic displacement parameters ($Å^2x10^3$) for $(IPA)_2(Tz)_2Pb_3Br_{10}$ at 293 K with estimated standard deviations in parentheses.

Label	U_{11}	U_{22}	U_{33}	U_{12}	U_{13}	U_{23}
Pb(1)	25(1)	26(1)	43(1)	-2(1)	2(1)	3(1)
Pb(2)	33(1)	31(1)	46(1)	-2(1)	9(1)	-2(1)
Pb(3)	35(1)	38(1)	61(1)	-5(1)	1(1)	9(1)
Br(1)	50(2)	52(2)	149(3)	-25(2)	16(2)	2(2)
Br(2)	132(3)	179(4)	44(2)	7(3)	7(2)	-18(2)
Br(3)	93(2)	182(5)	54(2)	7(2)	5(2)	5(2)
Br(4)	59(2)	56(2)	103(2)	22(2)	10(2)	2(2)
Br(5)	55(2)	42(2)	45(2)	9(2)	9(1)	5(2)
Br(6)	44(2)	48(2)	74(2)	22(2)	2(2)	-4(2)
Br(7)	53(2)	48(2)	84(2)	16(2)	18(2)	-2(2)
Br(8)	47(2)	43(2)	102(2)	-21(2)	21(2)	8(2)
Br(9)	54(2)	44(2)	157(3)	-27(2)	18(2)	-6(2)
Br(10)	118(2)	97(3)	42(2)	-9(2)	10(2)	0(2)

Table S11. Atomic coordinates ($x10^4$) and equivalent isotropic displacement parameters ($Å^2x10^3$) for $(PA)(Tz)PbBr_4$ at 293 K with estimated standard deviations in parentheses.

Label	x	y	z	Occupancy	U_{eq}^*
Pb(1)	3878(1)	4969(1)	5679(1)	1	29(1)
Pb(2)	1122(1)	5031(1)	10679(1)	1	29(1)
Br(3)	437(1)	5681(2)	10856(2)	1	39(1)
Br(4)	4563(1)	4318(2)	5856(2)	1	39(1)
Br(5)	1082(1)	2828(2)	7818(2)	1	46(1)
Br(6)	3919(1)	7171(2)	2817(2)	1	46(1)
Br(7)	3864(1)	2956(2)	8615(2)	1	52(1)
Br(8)	1136(1)	7044(2)	13615(2)	1	52(1)
Br(9)	3219(1)	5388(2)	5937(2)	1	58(1)
Br(10)	1781(1)	4612(2)	10937(2)	1	58(1)

Table S12. Anisotropic displacement parameters ($Å^2x10^3$) for $(PA)(Tz)PbBr_4$ at 293 K with estimated standard deviations in parentheses.

Label	U_{11}	U_{22}	U_{33}	U_{12}	U_{13}	U_{23}
Pb(1)	41(1)	23(1)	22(1)	1(1)	-2(1)	0(1)
Pb(2)	40(1)	23(1)	22(1)	1(1)	2(1)	0(1)
Br(3)	44(1)	44(1)	28(1)	-5(1)	0(1)	-1(1)
Br(4)	45(1)	43(1)	28(1)	-5(1)	0(1)	1(1)
Br(5)	59(1)	40(1)	39(1)	9(1)	-4(1)	-17(1)
Br(6)	59(1)	40(1)	39(1)	10(1)	4(1)	17(1)
Br(7)	68(2)	46(1)	43(1)	10(1)	6(1)	24(1)
Br(8)	69(2)	46(1)	43(1)	8(1)	-6(1)	-24(1)
Br(9)	44(1)	62(2)	69(2)	-5(1)	-3(1)	2(1)
Br(10)	43(1)	62(2)	69(2)	-4(1)	4(1)	-2(1)

Table S13. Atomic coordinates ($x10^4$) and equivalent isotropic displacement parameters ($Å^2x10^3$) for (BA)(Tz)$PbBr_4$ at 293 K with estimated standard deviations in parentheses.

Label	x	y	z	Occupancy	U_{eq}^*
Pb(1)	3937(1)	4967(1)	4320(1)	1	27(1)
Pb(2)	1063(1)	5033(1)	-680(1)	1	27(1)
Br(3)	4586(1)	4323(2)	4145(2)	1	37(1)
Br(4)	414(1)	5677(2)	-856(2)	1	37(1)
Br(5)	1023(1)	2825(2)	2186(2)	1	42(1)
Br(6)	3977(1)	7175(2)	7186(2)	1	42(1)
Br(7)	1073(1)	7039(2)	-3616(2)	1	49(1)
Br(8)	3927(1)	2961(2)	1384(2)	1	49(1)
Br(9)	1689(1)	4604(2)	-966(2)	1	52(1)
Br(10)	3312(1)	5396(2)	4034(2)	1	52(1)

Table S14. Anisotropic displacement parameters ($Å^2x10^3$) for (BA)(Tz)$PbBr_4$ at 296.15 K with estimated standard deviations in parentheses.

Label	U_{11}	U_{22}	U_{33}	U_{12}	U_{13}	U_{23}
Pb(1)	36(1)	22(1)	22(1)	1(1)	2(1)	0(1)
Pb(2)	36(1)	22(1)	22(1)	1(1)	-1(1)	0(1)
Br(3)	41(1)	43(1)	28(1)	-5(1)	0(1)	-1(1)
Br(4)	40(1)	43(1)	28(1)	-5(1)	1(1)	1(1)
Br(5)	52(1)	38(1)	36(1)	9(1)	4(1)	15(1)
Br(6)	52(1)	38(1)	36(1)	8(1)	-3(1)	-14(1)
Br(7)	63(1)	44(1)	41(1)	9(1)	6(1)	22(1)
Br(8)	64(1)	44(1)	41(1)	9(1)	-6(1)	-22(1)
Br(9)	40(1)	56(1)	59(1)	-6(1)	-3(1)	2(1)
Br(10)	39(1)	56(1)	59(1)	-6(1)	4(1)	-2(1)

Table S15. Atomic coordinates ($x10^4$) and equivalent isotropic displacement parameters ($Å^2x10^3$) for $(PA)_2PbBr_4$ at 293 K with estimated standard deviations in parentheses.

Label	x	y	z	Occupancy	U_{eq}^*
Pb(1)	0	0	0	1	41(1)
Br(1)	-1923(1)	3082(2)	26(1)	1	59(1)
Br(2)	323(2)	179(2)	1192(1)	1	66(1)

Table S16. Anisotropic displacement parameters ($Å^2x10^3$) for $(PA)_2PbBr_4$ at 293 K with estimated standard deviations in parentheses.

Label	U_{11}	U_{22}	U_{33}	U_{12}	U_{13}	U_{23}
Pb(1)	32(1)	31(1)	61(1)	0(1)	0(1)	1(1)
Br(1)	46(1)	44(1)	88(1)	17(1)	-9(1)	-3(1)
Br(2)	66(1)	69(1)	63(1)	-2(1)	6(1)	3(1)

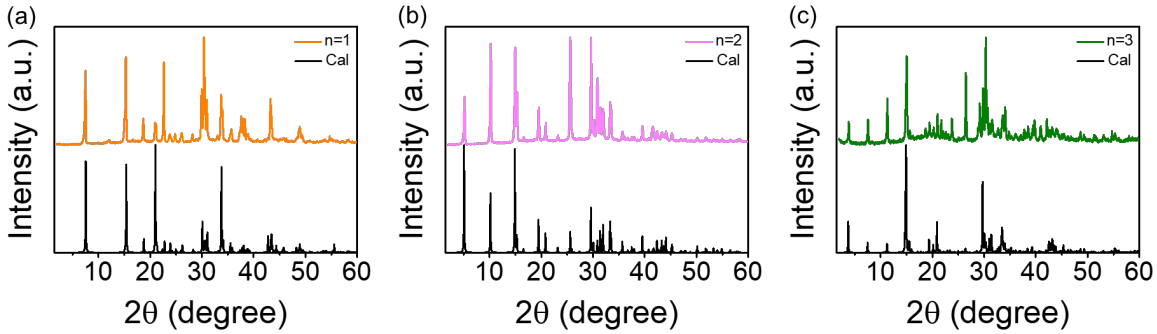

Figure S1. PXRD patterns for the $(IPA)_2(Tz)_{n-1}Pb_nBr_{3n+1}$ (n = 1–3) series. (a) n = 1, (b) n = 2 and (c) n = 3.

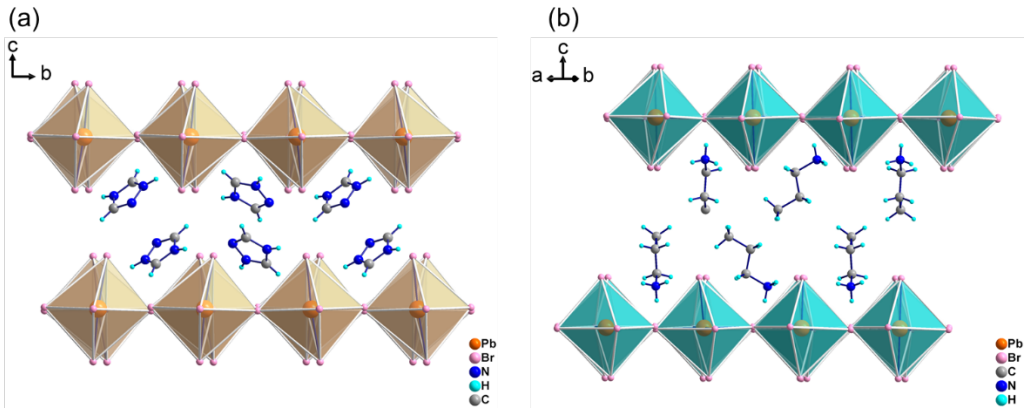

Figure S2. Crystal structures of (a) $(Tz)_2PbBr_4$ and (b) $(PA)_2PbBr_4$.

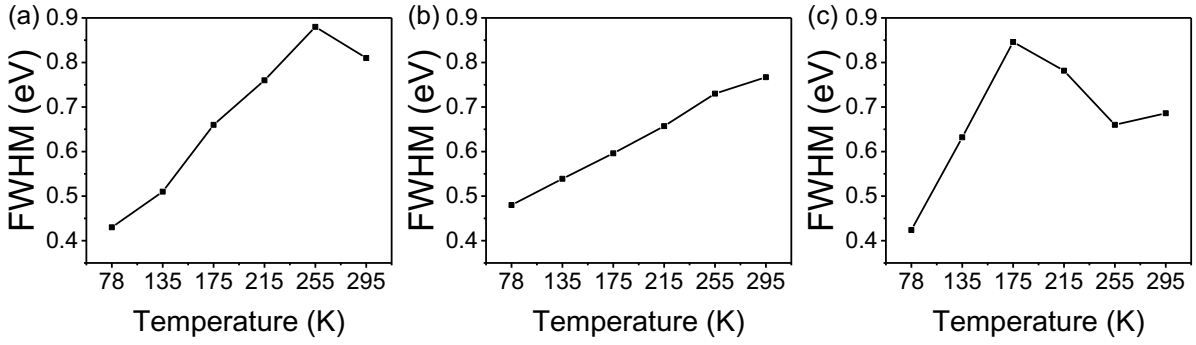

Figure S3. Full width at half maximum (FWHM) of the PL spectra of the $(IPA)_2(Tz)_{n-1}Pb_nBr_{3n+1}$ (n = 1–3) series. (a) n = 1, (b) n = 2 and (c) n = 3.

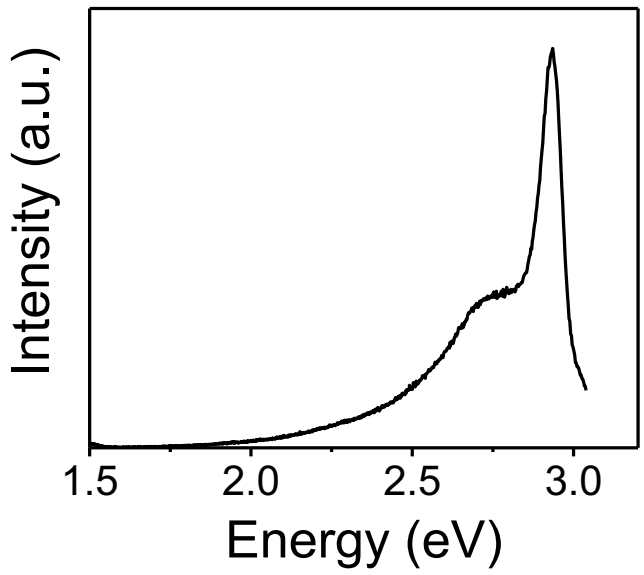

Figure S4. Room-temperature PL spectrum of (PA)(Tz)$PbBr_4$ (FWHM is 0.1 eV).

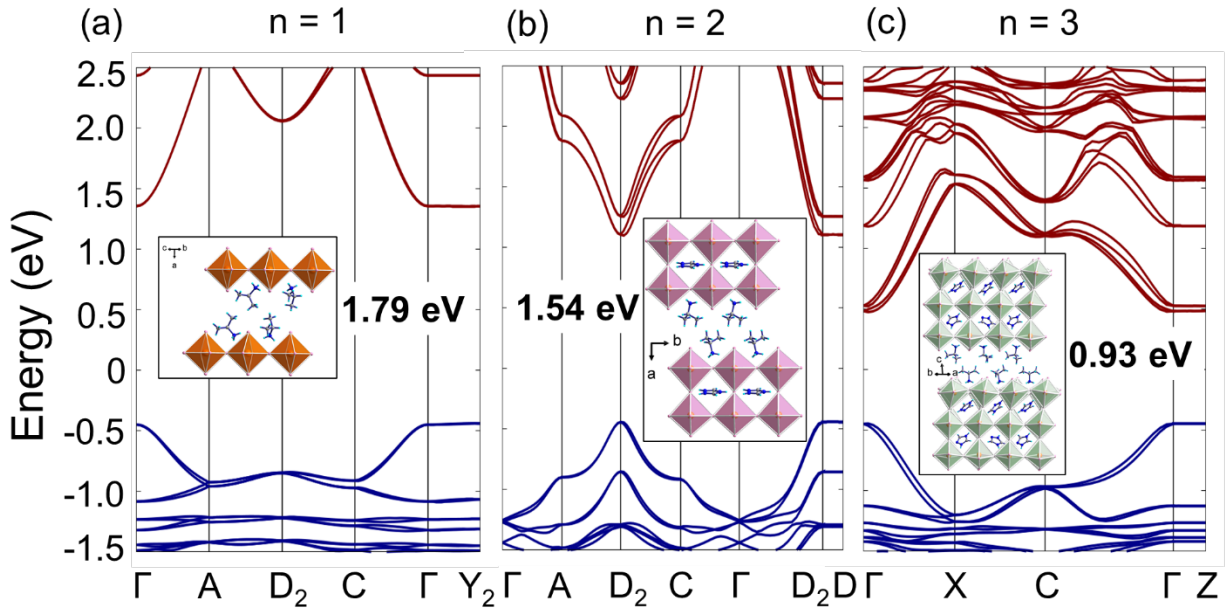

Figure S5. DFT-PBE electronic band structures of the $(IPA)_2(Tz)_{n-1}Pb_nBr_{3n+1}$ (n = 1–3) series. (a) n = 1, (b) n = 2 and (c) n = 3.

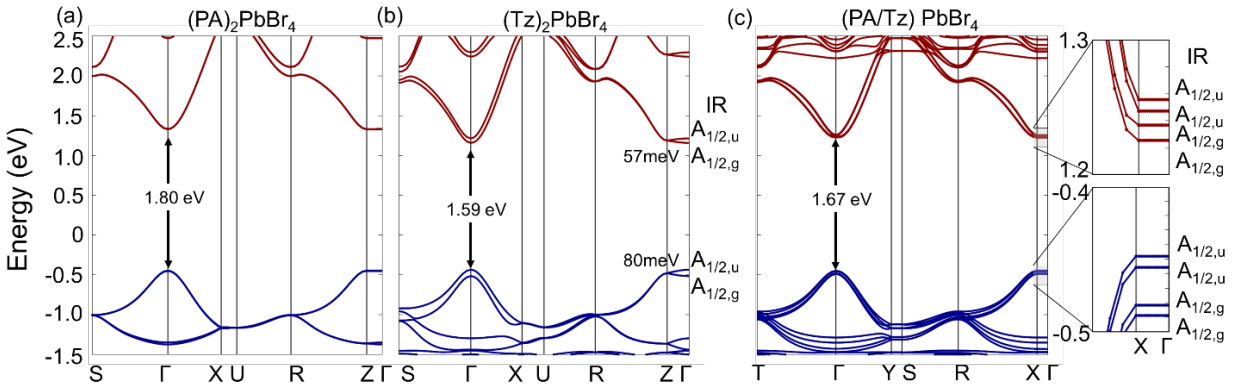

Figure S6. DFT-PBE electronic band structures of (a) $(PA)_2PbBr_4$, (b) $(Tz)_2PbBr_4$ and (c) (PA)(Tz)$PbBr_4$, showing the irreducible representations at the electronic bands near the band edges.

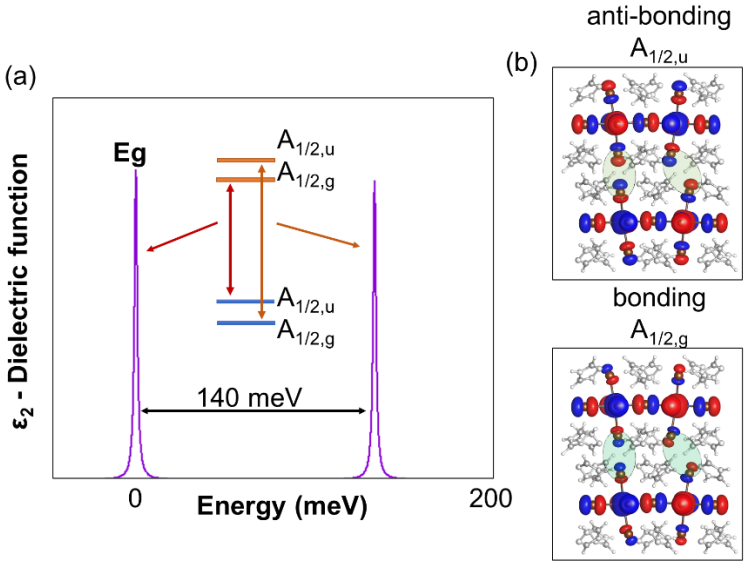

Figure S7. (a) Calculated imaginary part of the dielectric function for $(Tz)_2PbBr_4$ near the absorption onset. Inset: schematic diagram showing the symmetry allowed transitions and related irreducible representations that correspond to the two observed peaks. (b) Partial density of states (PDOS) of $(Tz)_2PbBr_4$ at the valence band edge. Shaded areas highlight the wavefunction signs showing the bonding and anti-bonding interaction between the layers.

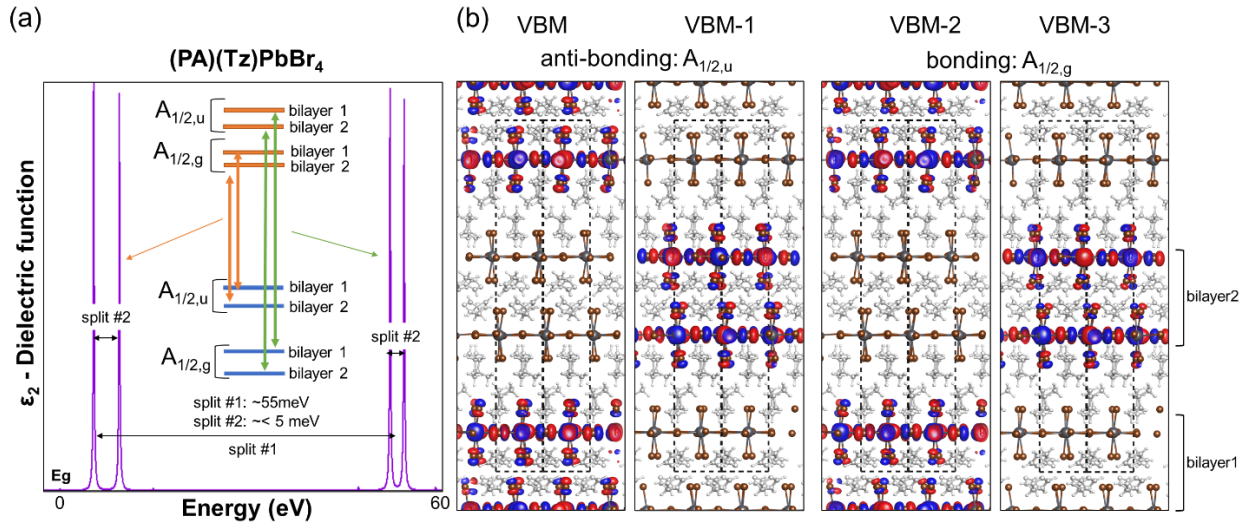

Figure S8. (a) Calculated imaginary part of the dielectric function for (PA)(Tz)$PbBr_4$ near the absorption onset. Inset: schematic diagram showing the symmetry allowed transitions, and related irreducible representations, that correspond to the four observed peaks, and (b) Pseudo charge density plot for the valence band maximum (VBM), and the three lower bands (VBM-1, VBM-2, VBM-3) of (PA)(Tz)$PbBr_4$, showing the origin of the observed band splits.

References:

[1] G. Kresse and J. Furthmüller, Phys. Rev. B **1996**, *54*, 11169.

[2] P. Gianozzi et al., J. Chem. Phys. **2020**, *152*, 154105.

[3] D Sangalli et al., J. Phys.: Condens. Matter **2019**, *31*, 325902.

[4] P. E. Blöchl, Phys. Rev. B **1994**, *50*, 17953.

[5] J. P. Perdew, K. Burke, M. Ernzerhof, Phys. Rev. Lett. **1996**, *77*, 3865.

[6] C. Adamo, V. Barone, J. Chem. Phys. **1999**, *110*, 6158.

[7] M. J. van Setten, Comp. Phys. Comm. **2018**, *226*, 39.